AD-A114 376 BEERS (ROLAND F) INC ALEXANDRIA VA F/G 20/8
ELECTRON BEAM TRANSPORT IN THE IONOSPHERE - ENERGY DEPOSITION A--ETC(U)
FEB 82 D J STRICKLAND, D L LIN, V W PINE F19628-81-C-0048
UNCLASSIFIED AFGL-TR-82-0083 NL

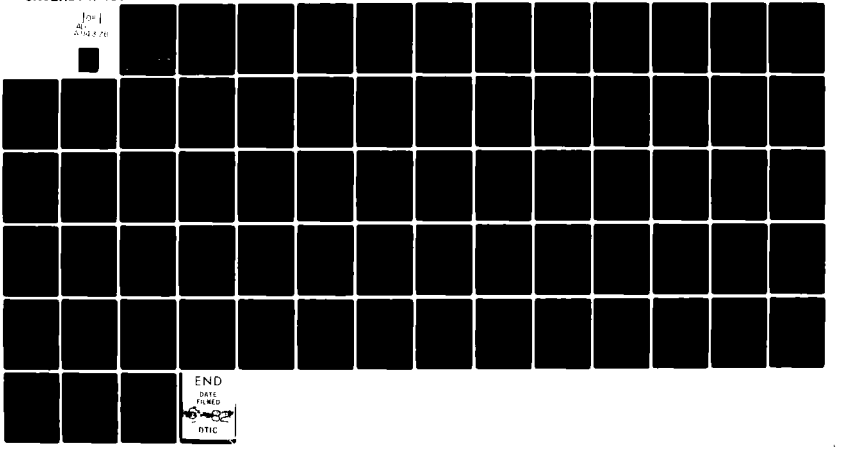

END
DATE FILMED
DTIC

(12)

AFGL-TR-82-0083

ELECTRON BEAM TRANSPORT IN THE IONOSPHERE - ENERGY DEPOSITION AND OPTICAL EMISSIONS BASED UPON THE COMBINED EFFECTS OF PLASMA TURBULENCE AND PARTICLE-PARTICLE INTERACTIONS

D.J. Strickland
D.L. Lin
V.W. Pine
M.J. Schmidt

Beers Associates, Inc.
P.O. Box 2549
Reston, Virginia

Final Report
January 1981 - December 1981

February 1982

Approved for public release; distribution unlimited

AIR FORCE GEOPHYSICS LABORATORY
AIR FORCE SYSTEMS COMMAND
UNITED STATES AIR FORCE
HANSCOM AFB, MASSACHUSETTS 01731

Unclassified
SECURITY CLASSIFICATION OF THIS PAGE (When Data Entered)

REPORT DOCUMENTATION PAGE	READ INSTRUCTIONS BEFORE COMPLETING FORM
1 REPORT NUMBER: AFGL-TR-82-0083	2 GOVT ACCESSION NO: AD-A114 376
	3 RECIPIENT'S CATALOG NUMBER
4 TITLE (and Subtitle): Electron Beam Transport in the Ionosphere - Energy Deposition and Optical Emissions Based Upon the Combined Effects of Plasma Turbulence and Particle-Particle Interactions	5 TYPE OF REPORT & PERIOD COVERED: Final-81 Jan. to 81 Dec.
	6 PERFORMING ORG. REPORT NUMBER
7 AUTHOR(s): D.J. Strickland, D.L. Lin, V.W. Pine & M.J. Schmidt*	8 CONTRACT OR GRANT NUMBER(s): F19628-81-C-0048
9 PERFORMING ORGANIZATION NAME AND ADDRESS: Beers Associates, Inc. P.O. Box 2549 Reston, Virginia	10 PROGRAM ELEMENT, PROJECT, TASK AREA & WORK UNIT NUMBERS: 62101F 7601 15BA
11 CONTROLLING OFFICE NAME AND ADDRESS: Air Force Geophysics Laboratory Hanscom Air Force Base, Mass. 01731 Monitor/Frederick Innes/PHG	12 REPORT DATE: February, 1982
	13 NUMBER OF PAGES: 70
14 MONITORING AGENCY NAME & ADDRESS (if different from Controlling Office)	15 SECURITY CLASS. (of this report): Unclassified
	15a DECLASSIFICATION/DOWNGRADING SCHEDULE

16 DISTRIBUTION STATEMENT (of this Report)

Approved for public release; distribution unlimited

17 DISTRIBUTION STATEMENT (of the abstract entered in Block 20, if different from Report)

18 SUPPLEMENTARY NOTES

*Science Applications, Inc.

19 KEY WORDS (Continue on reverse side if necessary and identify by block number)

Electron Beams, E-Region, Particle-Particle Interactions, Plasma Turbulence, Beam Propagation

20 ABSTRACT (Continue on reverse side if necessary and identify by block number)

The problem of electron beam propagation in the E-region is examined. A model is developed to describe that part of beam spreading due to plasma turbulence. The basis of the model is that the given turbulence can cause a series of effective displacements Δr_{GC} of the beam electron guiding centers through a corresponding series of briefly experienced perpendicular

DD FORM 1 JAN 73 1473 EDITION OF 1 NOV 65 IS OBSOLETE

Unclassified
SECURITY CLASSIFICATION OF THIS PAGE (When Data Entered)

Unclassified

SECURITY CLASSIFICATION OF THIS PAGE (When Data Entered)

components of the turbulent electric field. Weak turbulence theory is considered and applied to cases of warm and cold beams. A Monte Carlo code has been developed to follow the spreading of the beam electron guiding centers where Δr_{GC} is given altitude dependence. An analytic expression is used when Δr_{GC} is constant with altitude. The turbulence model is used to examine beam spreading as observed by Davis et al. (1971) and Hallinan et al. (1978). We can generally account for the observed amount of spreading by adding in the contribution due to particle-particle interactions. Optical properties associated with beam energy deposition are also modeled. Most features in the UV and visible portion of the optical spectrum are considered along with their emission efficiences. Summed intensities of these features are given as functions of z and r. This is done for a 38 keV beam similar to one generated in the ECHO IV experiment. Turbulence and particle-particle interactions are modeled in the calculations.

Unclassified

SECURITY CLASSIFICATION OF THIS PAGE (When Data Entered)

TABLE OF CONTENTS

Section 1

INTRODUCTION AND SUMMARY

This is the final report on AFGL Contract F19628-81-C-0048 titled "Electron Beam Transport in the Ionosphere - Energy Deposition and Optical Emissions Based Upon the Combined Effects of Plasma Turbulence and Particle-Particle Interactions". This work has been carried out for the Air Force in support of planned rocket and satellite kilovolt electron beam (e-beam) experiments. Our goals in this program have been to

1) model plasma turbulence as it affects kilovolt e-beams in the E-region,

and

2) make quantitative estimates of beam energy deposition and luminosity as functions of altitude z and radial distance r.

This work is an extension of our efforts under a previous contract in which code MCBE was developed and applied to the problem of particle-particle interactions. MCBE is a 2D Monte Carlo code explicitly treating electron motion in a magnetic field. Energy loss is approximated as continuous and beam spreading comes about by use of a multiple-scattering formula.

Particle-particle interactions are not sufficient to cause the spreading observed in some beam produced luminosity streaks of past experiments. (Davis et al. (1971) and Hallinan et al. (1978)). We were able to determine the extent of this deficiency in our earlier work using MCBE. It is clear from this work as well as from an examination of Hallinan's data that plasma turbulence can play an important role in e-beam propagation in the E-region. Much of our effort under the current contract has been to quantify the effect of this turbulence.

It is helpful to briefly outline the approach we have taken in modeling beam-plasma interactions prior to presenting the details in Sections 2 and 3. We first assume the wave-particle and particle-particle regions can be effectively separated. The basis of the model is then that the given turbulence can cause a series of effective displacements of the beam electron guiding centers through a corresponding series of briefly experienced perpendicular components of the turbulent electric field, $E_\perp$. The lower altitude boundary for this effect is defined as the altitude at which the turbulent growth rate equals the particle-particle collision frequency. Above this altitude, we use a Monte Carlo description to follow the motions of the beam electron guiding centers caused by the above mentioned displacements if they are given altitude dependence. Otherwise, the final result of the displacements is given by an analytical radial distribution function (Gaussian).

A given displacement is a function of both $E_\perp$ and an autocorrelation time τ. We choose to replace $E_\perp$ by an expression containing δv, the velocity spread of the beam reflecting the strength of the turbulence. The nature of this quantity will be considered for both cold and warm beams. Emphasis will be on warm beams for which δv can be equated to the beam thermal velocity. Specification of δv for this case is made through the parameter β which gives the ratio of the thermal to the beam energy [$\beta = (\delta v/v)^2$]. Spreading is then examined for β ranging from .01 to .1 with the guiding center displacement being constant versus altitude. It is difficult to prescribe the beam thermal velocity. For this reason we have chosen limiting values of β for a given beam so as to bound the beam spread. This scoping approach to the problem is further justified because of the large uncertainties in the experimental measurements.

Following the above introductory remarks, we summarize our results as follows:

1) A model has been developed which provides for beam spreading by plasma turbulence. The model is based on random walk motion of the beam electron guiding centers caused by the perpendicular component of the turbulent electric field.

2) The model has been used in an analysis of beam spreading reported by Hallinan et al. (1978) [ECHO IV experiment] and Davis et al. (1971). We can account for most beam widths by adding the additional spreading due to particle-particle effects. For the pulses injected below 180 km, our fits suggest a β value $\leq .01$.

3) Detailed energy deposition results (in r and z) are presented for two of the beam cases considered. The results come from code MCBE for incident radial distributions given by a delta function and by the above mentioned turbulence model.

4) Optical properties of the beams treated in 3) are determined. These include r,z distributions of surface brightness for the sum of most emission features in the UV and visible portions of the optical spectrum. Scaling factors are also provided which relate emission efficiencies to energy deposition for the individual features just mentioned.

As a concluding remark, the work carried out in this program together with that from the earlier one enables us to examine the r,z dependence of energy deposition and optical emissions for electron beams propagating through the E-region under the influence of particle-particle interactions and plasma turbulence.

Section 2

RANDOM WALK MODEL FOR WAVE-PARTICLE INTERACTIONS

In this section, we will describe the random walk of the guiding center of the beam electrons due to wave-particle interactions. This type of treatment is meant to place the mechanism of the spreading caused by wave-particle interactions on the same footing as that for particle-particle interactions; the details of the latter have been given by Lin and Strickland (1981). In the case of particle-particle interactions, the random force is provided by collisions between beam electrons and neutral particles. For wave-particle interactions, the random force is due to the turbulent E field acting on the beam electrons.

2.1 Guiding Center Motion.

Let $\vec{B}$ be the magnetic field and $\hat{z}$ the direction of $\vec{B}$. The equation of motion of a beam electron is given by

$$\frac{d\vec{v}}{dt} = \frac{e\vec{v} \times \vec{B}}{mc} + \frac{e\vec{E}}{m} \tag{1}$$

We are not interested in the coordinates of the beam electron; instead, what concerns us are the coordinates of its guiding center. In the x-y plane, the electron is positioned at (x,y) with velocity (v_x,v_y) while its guiding center is at $\vec{r}_{GC} = (x_{GC},y_{GC})$. They are related by

$$x_{GC} = x - v_y/ \tag{2}$$

$$y_{GC} = y + v_x/ \tag{3}$$

where Ω is the gyrofrequency.

Taking the perpendicular component (i.e., the component in the x-y plane) of Equation (1) and using Equations (2) and (3), we arrive at

$$\frac{d\vec{r}_{GC}}{dt} = \frac{e\vec{E}_{\perp}}{m\Omega} \tag{4}$$

or

$$\Delta r_{GC} = \frac{eE_{\perp}}{m\Omega} \tau \ , \tag{5}$$

where $E_{\perp}$ is now the perpendicular component of the turbulent E field and τ is the time interval for a coherent interaction (the auto-correlation time).

Equation (5) is the basis for our random walk model for wave particle interactions. It can also be derived using the $\vec{E}X\vec{B}$ drift velocity $\vec{E}X\vec{B}/cB^2$ to get $\Delta r = v_{drift}\, \tau$. The picture of the random walk of the guiding center is described in the following subsection.

2.2 Spatial Properties of the Turbulence Model.

The turbulent plasma is considered to contain regions of appreciable electric field strengths. Within each region, phase coherence is maintained in the manner described by Stix (1964). The phase of oscillations in one region is random with respect to the phase in each other region due to nonlinear effects of the large-amplitude disturbance. The length within which coherence is maintained is called the correlation length. (Stix's analysis results in a correlation length of about 0.64 λ where λ is the effective wavelength of the turbulence).

In a correlation length, the beam electron sees a constant E field (see Appendix B for details). Each of the three dimensions of a

coherent region is about one correlation length. Thus, the beam electrons feel the constant E field during the time they traverse a correlation length and then run into another coherent region where they feel another constant E-field whose phase is random with respect to the E field in the previous coherent region, and so on. The guiding center accordingly undergoes a random walk motion such that the beam spreads.

2.3 Displacement Δr_{GC} as a Function of Turbulent Velocity δv.

We first define needed quantities associated with the coherency of the turbulent spectrum. The correlation length ℓ is given by

$$\ell = C_1 \lambda \tag{6}$$

and the coherency time by

$$\tau = \ell / v_b \tag{7}$$

The above expressions are appropriate for coherent wave packets with group velocities much smaller than the beam velocity. The value of C_1 is of order unity with its specific value given by the applied turbulence model.

The potential energy of the turbulent electrostatic mode can be written

$$e\phi = 8\sqrt{2}\,[\tfrac{1}{2} m(\delta v)^2] \tag{8}$$

where the velocity δv is an equivalent measure of the strength of the turbulence. The numerical factor in Equation (8) corresponds to the result of Drummond et al. (1970). For cold beam-weak turbulence, $\delta v = v_{b_\parallel} - \omega/k_\parallel$ as discussed by Drummond et al. (1970) and O'Neil et al (1971). For strong turbulence, $\delta v = v_b/4\sqrt{2}$ as described by Stix (1964). We assume the cold beam-weak turbulence form can also be applied to the warm beam-weak turbulence case which shall be of particular interest to us. In Section 3.1, this will lead to δv being equated to the beam thermal velocity.

The wave-particle interaction is a collisionless effect. Mode damping will occur when particle-particle interactions become large enough at the lower altitudes. This limiting particle-particle frequency can be written

$$\gamma\,(\text{particle-particle collision}) = C_2\gamma, \tag{9}$$

where γ is the linear growth and C_2 is of order unity.

Let θ_k be the angle between $\vec{k}$ and $\vec{B}$ and θ_b the angle between $\vec{v}_b$ and $\vec{B}$. We introduce an effective gyroradius r_g:

$$r_g = v_b/\Omega \tag{10}$$

which is defined independent of the angle θ_b.

With the use of Equations (6), (7), (8), and (10) we can write Equation (5) in the form

$$\frac{\Delta r_{GC}}{r_g} = 8\sqrt{2}\,\pi C_1 \sin\theta_k \left(\frac{\delta v}{v_b}\right)^2 \tag{11}$$

Use is made of $E_\perp = E_\parallel \tan\theta_k$, $\delta k_\parallel = E_\parallel$, and $k\lambda = 2\pi$. To apply Equation (11) to a specific problem, we must provide a specification to δv which will be done in Section 3.

2.4 Radial Distribution Function and Avearge Beam Radius.

In this subsection, we discuss the two cases where Δr_{GC} is constant and variable. For the case of constant Δr_{GC}, the needed function for the beam radial distribution after N displacements of the guiding center is analytical. For the other case, a numerical procedure is called for, and this has been developed by us during this program. Details now follow.

We begin by defining N, the total number of steps or guiding center displacements caused by the turbulence. It is

$$N = \frac{t}{\tau} \tag{12}$$

where t is the travel time of the beam electrons within the region where the wave-particle interaction is dominant. Since the parallel wave phase velocity is equal to the corresponding component of the beam velocity in the types of plasma turbulence to be considered, viz.

$$\omega/k_{\parallel} = v_b \cos \theta_b , \tag{13}$$

we can write the coherence time in terms of the wave frequency:

$$\tau = 2\pi C_1 \cos \theta_k \cos \theta_b/\omega . \tag{14}$$

If we let d be the distance between the injection altitude and the altitude at which the particle-particle collision frequency is C_2 times the linear growth rate, then $t = d/V_b \cos \theta_b$ and we obtain

$$N = \frac{1}{C_1 2\pi \cos \theta_k \cos^2 \theta_b} \left(\frac{\omega d}{v_b}\right) \tag{15}$$

A typical case of $\omega = 6 \times 10^6$ sec^{-1}, d = 50 km, $mv_b^2/2 = 26$ keV, $\theta_k = 45^0$, and $\theta_b = 70^0$ generates an N of 8512 if $C_1 = 1$.

Let $W_N(r)$ designate the radial distribution function after N displacements where N refers to an average for each of the beam particles. For constant Δr_{GC}, $W_N(r)$ has the form

$$W_N(r) = \left[\pi N \left(\frac{\Delta r_{GC}}{r_g}\right)^2\right]^{-1} \exp - \left(\frac{r^2}{N\left(\frac{\Delta r_{GC}}{r_g}\right)^2}\right) \qquad (16)$$

with normalization

$$\int_0^\infty W_N(r)\, 2\pi r dr = 1 \; . \qquad (17)$$

$W_N(r)$ is the same distribution function given by Lin and Strickland (1981) for particle-particle interactions, except now Δr_{GC} is to be specified for wave-particle effects.

We may go one step further for the constant step size case and express analytically the average radius of the beam from Equation (16). Designating it by $\langle r \rangle_w$ (in units of r_g), it is

$$\langle r \rangle_w = \sqrt{\pi N}\, \frac{\Delta r_{GC}}{2 r_g} = 4\pi \sqrt{\frac{C_1}{\cos \theta_k}}\, \frac{\sin \theta_k}{\cos \theta_b} \sqrt{\frac{\omega d}{v_b}} \left(\frac{\delta v}{v_b}\right)^2 \qquad (18)$$

We will make use of Equations (16) and (18) in the next section as we discuss the ECHO IV experiment.

For non-constant Δr_{GC}, we have developed a Monte Carlo code (WPDIF) to describe the 2D random walking of the beam electron guiding centers. A brief description of the input parameters and calculation follows starting with the parameters. They are:

z_0	starting altitude
μ_0	cosine of the pitch angle of the starting beam electrons
E	electron energy
$n_p(z)$	altitude profile of the plasma density
I_b	starting beam current
f_0	starting distribution of guiding centers
M	number of histories or electrons to be sampled.

The value of M used to obtain our initial results is 1000. These M electrons are allowed to advance in their random motion as a group. Thus in passing through a given Δz corresponding to the coherence time τ, M guiding center displacements are determined and recorded. This enables us to specify the decreasing beam density at each step for input into the expression for the displacement through the next step. The calculation proceeds until the growth rate γ for the given instability is exceeded by the electron-neutral collision frequency.

This completes the formalism of our random walk model. We now turn to applications in which specification will be given to δv and N.

Section 3

APPLICATIONS OF THE RANDOM WALK MODEL

We now consider the level of plasma turbulence anticipated for beam parameters of interest. It is convenient to follow Davidson (1972) in defining two categories of beam driven turbulence. Weak turbulence corresponds to turbulent energy densities much smaller than the kinetic energy of the beam, whereas strong turbulence implies that a large portion of the beam energy is transferred to turbulence. Since beam energy losses to plasma turbulence have been found experimentally to be small, we consider weak turbulence in this report.

We distinguish two classes of weak turbulence by examining the linear theory of beam plasma instability. The growth rate depends on the beam temperature; if the temperature is sufficiently large, the condition for a warm beam is $v_{bth}/v_b \geq \alpha^{1/3}$, where v_{bth} is the beam thermal velocity and α is the ratio of the beam to ambient electron density. When the inequality is reversed, the beam is considered cold. It is difficult to access the values of the beam temperature. For cases where α is quite small, however, we assume the beam temperature can satisfy the above warm beam criterion. In what follows we apply the results of warm beam theory to the high energy-low current, and, thus, small α beams characteristic of the ECHO IV experiment (Hallinan et al. (1978)). On the other hand, we use cold beam theory to explain beam spreading in the rocket experiment reported by Davis et al. (1971) where a relatively low energy (8.7 keV) high current (500 mA) beam was injected.

3.1 Warm e-beam.

For warm beams, δv, is a constant and is equal to the beam thermal velocity v_{bth}. This may be seen using the linearized theory of the two-stream instability (see, e.g., Stix (1962)). The beam and the background plasma consist of a doubly-humped magnetized plasma which is vulnerable to the two-stream instability. The dispersion relation and the frequency are obtained by standard

methods (Stix (1964)). The wave number is obtained by maximizing $g'_b(v_\parallel)$ which is the derivative of the beam electron distribution function for the zero-order velocity component along B. The form of g_b is

$$g_b(v_\parallel) = \sqrt{\frac{m}{2\pi kT_{\parallel b}}} \quad \exp\left[-m(v_\parallel - v_{b_\parallel})^2/2kT_{\parallel b}\right] \tag{19}$$

The above maximizing leads to

$$w/k_\parallel = v_{b_\parallel} - v_{bth} \tag{20}$$

where $v_{bth} = \sqrt{kT_{\parallel b}/m}$. Equation (20) indicates that the parallel beam velocity is slightly greater than the parallel phase velocity by the amount of the beam thermal velocity. Recalling now the discussion following Equation (8), we see that Equation (20) leads us to the desired result, namely

$$\Delta v = v_{bth} \tag{21}$$

The magnitude of the constant step size is probably accurate during the initial stage of the beam spreading. This may not be as good an estimate at the final stage where the random walk suddenly stops. To make the transition smooth from the region where wave-particle interactions dominate to the region where particle-particle interactions dominate, we assume that the overall spreading of the beam is effectively the same as the case where the effective constant step size is half the maximum value given by Equation (11).

The beam radius as a function of the traveled vertical distance d can be identified with the mean beam radius. From Equation (18) we have

$$\langle r \rangle_w = A_1 \sqrt{d} \quad \left(\frac{v_{bth}}{v_b}\right)^2 . \tag{22}$$

where the final value of d is obtained by the criterion that the linear growth rate is the same as the collision frequency (we assume $C_2 = 1$).

It should be noted that A_1, as may be obtained from Equation (18) is here to be halved based on the comments of the previous paragraph. For a warm beam the linear growth rate is linearly proportional to α (Stix (1964) and Tsytovich (1977)).

$$\gamma = \frac{\pi}{2}\sqrt{\frac{2}{\pi\exp(1)}}\ \omega\alpha\left(\frac{v_b}{v_{bth}}\right)^2 Q(w) \tag{23}$$

where Q(w), a function discussed in Appendix A, is evaluated at its maximum. For parameters of interest, $Q_{max} \sim 0.4$. The important quantities of concern here are α and β. γ is expressed as

$$\gamma = A_2\,\alpha/\beta \tag{24}$$

where A_2 contains the terms in Equation (23) other than α and β with a Q value of .4. If we denote the initial value of γ by γ_0, then

$$\gamma_0 = A_2\,\alpha_0/\beta \tag{25}$$

and

$$\gamma = \gamma_0/(1+R)^2 = \gamma_0/(1+A_1\sqrt{d}\beta)^2 \tag{26}$$

where we have assumed the thermal energy of the beam remains the same and the beam initially has a radius of one equivalent gyroradius r_g.

Equation (26) gives the linear growth rate as a function of d. Final d, called d_f, is obtained by equating γ to the collision frequency.

The values of the parameters for ECHO IV experiments are assumed as follows:

$C_1 = 0.64$

$n_e = 10^5$ cm^{-3}

$\nu = 10^7$ sec^{-1}

The quantities ω and θ_k can be worked out following the method prescribed by Stix (1964). The resulting values are $\omega = 6 \times 10^6$ sec^{-1} and $\theta_k = 45^0$. Table 1 lists the values of parameters for all observed streaks in ECHO IV experiments. The values of α_0 are given for a beam density distributed uniformly out to the initial gyroradius r_g. The last column is the minimum value of $(v_{bth}/v_b)^2$ satisfying the warm beam condition. We see in all cases that our lower limit of .01 for β exceeds this required minimum value.

Table 1. Parameter Values of ECHO 4 Experiments

Pulse Number	Energy (keV)	α_0	θ_b	$\min(v_{bth}/v_b)^2$
12	38	.00023	60°	.0038
10	26	.00035	70°	.0050
21	34	.00036	70°	.0051
3	36	.00018	70°	.0032
24	33	.00042	70°	.0056
1	26	.00027	70°	.0042

The decreasing of the linear growth rate and the increasing of the collision frequency for the experimental parameters are shown in Figs. 1-3. Growth rates are shown for the two β values of .01 and .1. Two collision frequencies are also shown reflecting the uncertainty in the scattering cross section. This cross section is given by the screened Rutherford formula

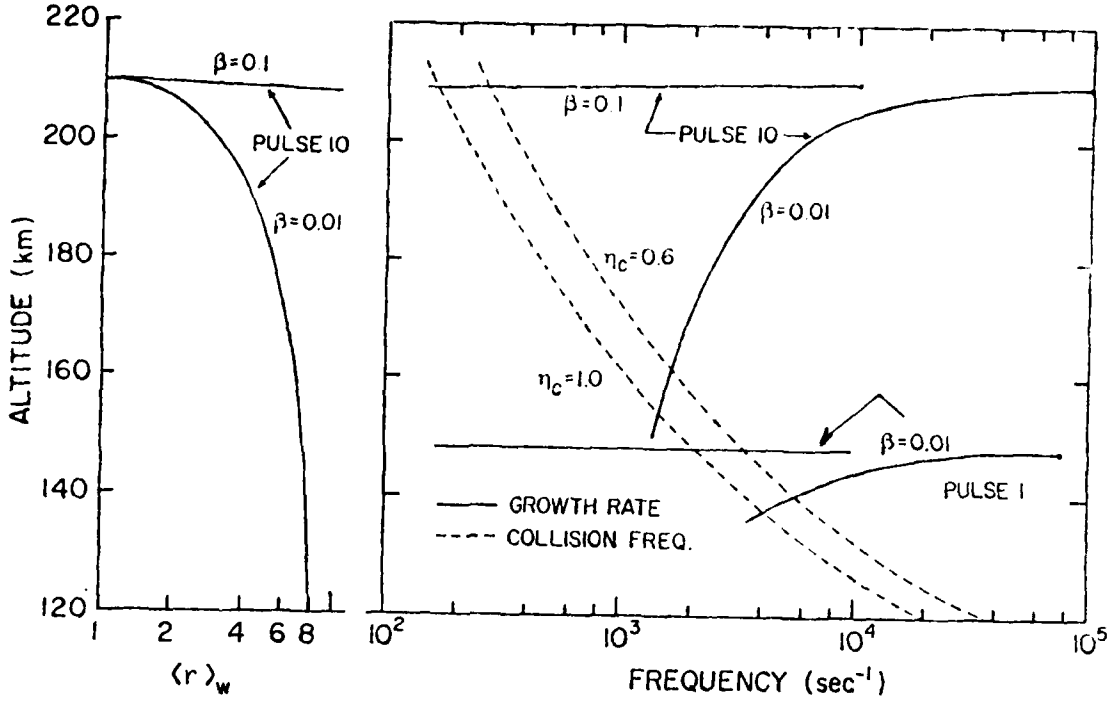

Figure 1. Growth Rate, Particle-Particle Collision Frequency, and Mean Beam Radius For Warm Beam Model Applied to Two of The ECHO IV e-Beams Labeled as Pulses 1 and 10. Only $\langle r \rangle_w$ for pulse 10 is shown since this part of the figure is to just illustrate the general behavior of the spreading with propagation distance.

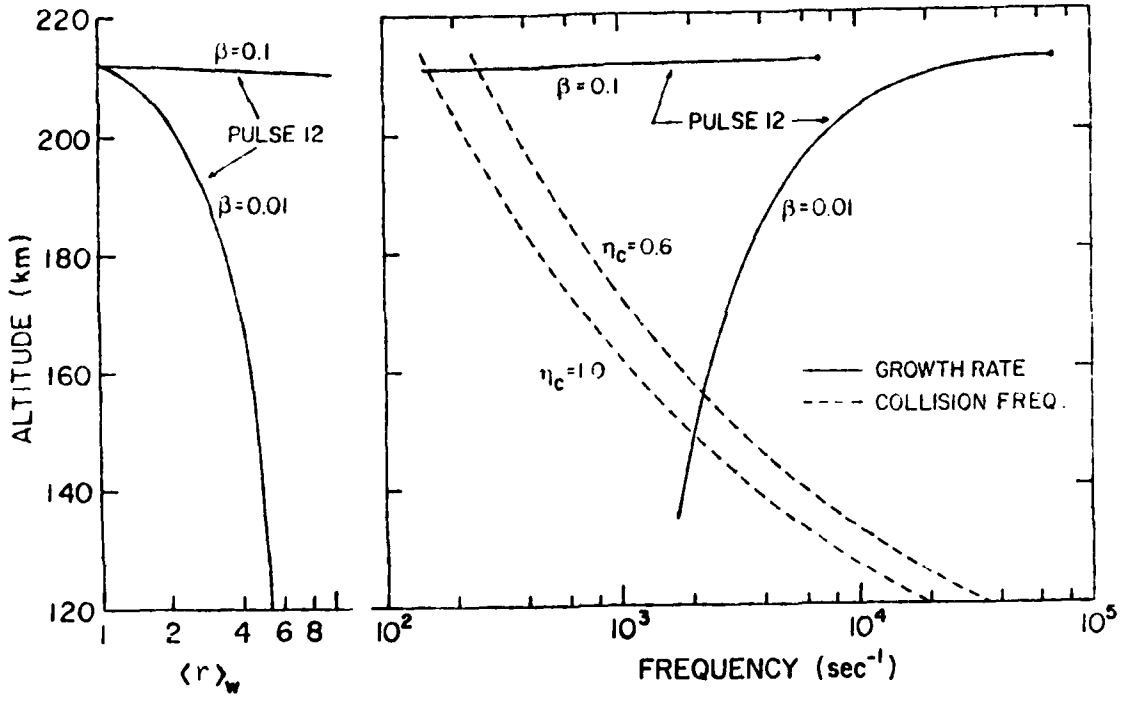

Figure 2. Similar to Figure 1 Except for Pulse 12.

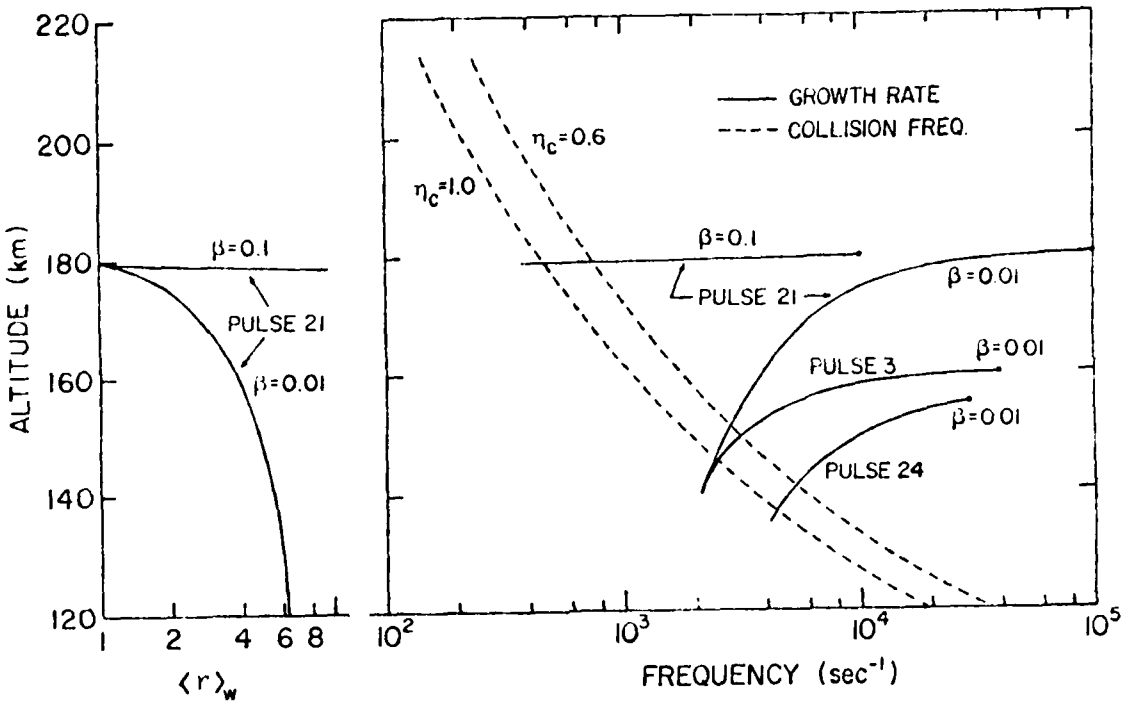

Figure 3. Similar to Figure 1 Except for Pulses 3, 21, and 24. Again, only one example of $\langle r \rangle_w$ is included as was the case in Figure 1.

$$\nu_{elas}(E) = \frac{Z^2 e^4}{v^2 p^2} \frac{\eta}{\eta(\eta + 1)} \tag{27}$$

where Z is the atomic number of the scatterer, v and p are the velocity and momentum of the incident electron, and η is a screening parameter. This latter quantity may be expressed in the form

$$\eta = \frac{4.3\, Z^{2/3}}{E} \eta_c \tag{28}$$

where η_c is constant and is dependent on the screening potential. Here, we consider two values of η_c (.6 and 1.0) chosen to reflect the uncertainty in this potential for our application (Berger et al. (1970)).

It is interesting to observe from these plots that the cutoff altitudes between the wave-particle dominant region and the particle-particle dominant region are about 150 km for all the ECHO IV experiments if β = .01. If β = .1, the cutoff altitude is slightly below the injection altitude.

The range of final beam radius for β ranging from .01 to .1 is presented in Table 2 for each experiment. The η_c value of .6 was used to specify the cut-off altitude. The spread for pulse 12 is narrower than that of the others and is due to a combination of its energy and injection pitch angle.

Table 2. Beam Spreading Due to Wave-Particle Interaction

Pulse Number	Energy (keV)	$\langle r \rangle_w$	d_f (km)
12	38	4.4 - 4.6	.524 - 56
10	26	4.6 - 6.6	.22 - 45
21	34	3 - 5	.1 - 28
3	36	.7 - 2.8	.006 - 10
24	33	1.3 - 3.4	.02 - 14
1	26	.33 - 2.4	.001 - 6

In Figure 4, we show the beam spreading due to particle-particle interactions (the solid vertical line) and the total spreading due to both particle-particle and wave-particle interactions (the shaded bars). Except for the 26 keV case injected at 210 km, good agreement is found for all the other cases between experiments and calculations.

3.2 Cold e-beam

We now consider the cold beam model for the case of the 8.7 keV, 500 mA beam in the Davis et al. (1971) experiment. Linear theory, giving the dispersion relation for cold beams injected into a plasma, predicts (O'Neil and Malmberg (1968)) the following maximum growth rate

$$\gamma = \frac{\sqrt{3}}{2} \left(\frac{\omega}{2}\right)^{1/3} \omega_p \, r_g \tag{29}$$

where ω_p is the plasma frequency.
The electric field corresponding to the nonlinear development of the beam-plasma instability was given by Drummond et al. (1970) and O'Neil et al. (1971):

$$\frac{E^2}{8\pi} = \frac{1}{2} \left(\frac{\omega}{2}\right)^{1/3} \left(\frac{1}{2} n_b m v_b^2\right) \tag{30}$$

which can be derived by the usual particle trapping and bounce frequency arguments. For this case, δv is given by

$$\delta v = v_b - \frac{\omega}{k} = \frac{1}{2} \left(\frac{\omega}{2}\right)^{1/3} v_b \tag{31}$$

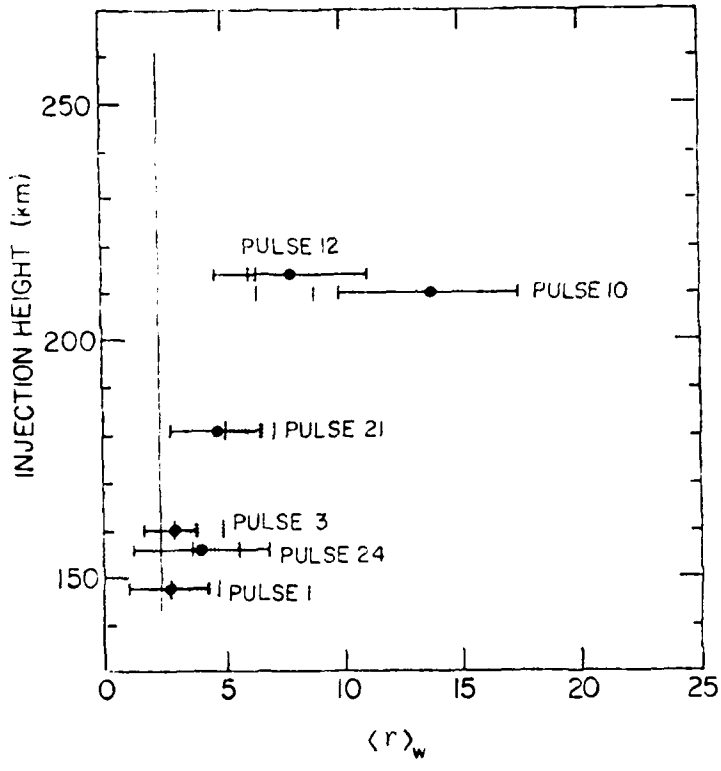

Figure 4. Mean Beam Radii For ECHO IV e-Beams. The Vertical Line is From Lin and Strickland (1981) and Gives the Approximate Particle-Particle Contribution. The Points and Error Bars Come From Hallinan et al. (1978). The Shaded Regions Give the Model Results for β Ranging From .01 to .1. The Particle-Particle Contribution is Included in These Results.

Substituting this equation into Equation (11), we get

$$\frac{(\Delta r)_{GC}}{r_g} = 2.\overline{2} \cdot C_1 \sin \phi_k \left(\frac{\omega}{2}\right)^{2/3} \tag{32}$$

Now,

$$\omega = 0.011 \frac{I(mA)}{E(keV)^{3/2}\, r^2} \tag{33}$$

where I(mA) is the current in mA, E(keV) is the energy in keV, and r is beam radius in r_g units. Thus,

$$\frac{(\Delta r)_{GC}}{r_g} = .275\, C_1 \sin \phi_k \frac{I(mA)^{2/3}}{E(keV)\, \tilde{r}^{4/3}} \tag{34}$$

and

$$\gamma = .152 \frac{I(mA)^{1/3}}{E(keV)^{1/2} r^{2/3}} \omega_p. \tag{35}$$

For the 8.7 keV case, I(mA) = 500. The background plasma is characterized by $\omega_p = 1.78 \times 10^6$ sec^{-1} when $n_e = 10^5$ cm^{-3}.

Since Δr_{CG} is not constant for the cold beam case, a numerical calculation of beam spreading has been performed using the Monte Carlo code described in Section 2.4. The results are shown in Figure 5 and, compared to the warm beam results of Figures 1 - 3, suggest that the wave-particle interaction

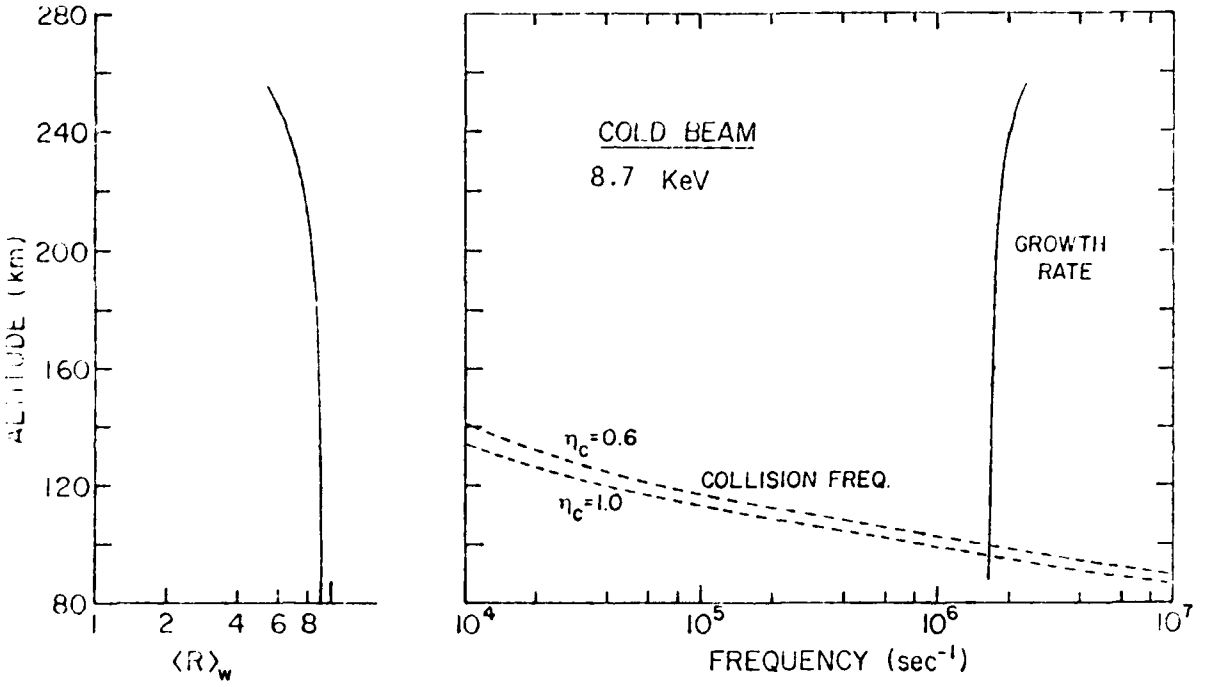

Figure 5. Similar to Figure 1 Except for the Cold Beam Case and the Experiment of Davis et al. (1971).

region extends much deeper into the atmosphere.

While the computed large beam spread indicates the importance of beam plasma turbulence, the results are not completely self-consistent. The appreciable beam expansion means α is greatly reduced, so that it is unlikely that the beam can remain cold at lower E-region altitudes. Thus Equations (29) and (30) should be replaced with warm beam expressions somewhere above 100 km. The intersection of γ and ν occurs at low altitudes, but there is a problem with performing the given calculation down to low altitudes due to energy loss. Significant loss will occur below 120 km, and this is not accounted for in the calculation. Thus our results should serve simply as an indication of the potential of turbulence in spreading the beam under discussion.

Section 4

DETAILED ENERGY DEPOSITION AND OPTICAL EMISSION PROPERTIES USING CODE MCBE

4.1 Computational Model and Problem Parameters.

In the previous section, we presented results basically analytical in nature giving the mean radius of selected e-beams following spreading due to turbulence and particle-particle interactions. The contribution from the latter effect was determined by using the analytical result of Lin and Strickland (1981) shown as the vertical line in Figure 4. In this section, we augment these analytical results with more detailed results from code MCBE. These will include 2D (r,z) contours of energy deposition and various other related quantities such as the mean radius of energy deposition.

Results will be shown for particle-particle interactions alone as well as for the combined effects of wave-particle and particle-particle interactions. We wish to make it clear that we have separated the regimes for these processes. Thus, MCBE accounts for beam spreading by wave-particle interactions through specification of the radial beam profile at its upper altitude boundary. The beam profile is calculated by the model specified in Section 2 which is implemented in the code WPDIF.

Code MCBE was developed for AFGL under a previous contract. The MCBE code describes the transport of electrons in the earth's atmosphere and includes the effects of the earth's magnetic field. The code solves the transport problem using an extension developed by D. L. Lin of the Monte Carlo simulation of multiple scattering originally developed by Berger (1963).

Results are to be presented for the two beam energies 8.7 keV and 38 keV. The initial radial distribution for the 8.7 keV beam is shown on the top graph of Figure 6. Initial distribution 1 is the distribution for the case neglecting wave particle effects. Initial distribution 2 is the distribution for the case including the effects of wave-particle interactions. Other parameters pertinent to the 8.7 keV MCBE calculations are summarized in Table 3 below.

	Neglecting Wave-Particle Effects	Including Wave-Particle Effects
Distribution	1	2
Initial Altitude	260 km	120 km
Initial Angle	70° wrt $\vec{B}_{earth}$	70° wrt $\vec{B}_{earth}$
$\|\vec{B}_{earth}\|$	.5 gauss	.5 gauss

Table 3. Summary of Input Parameters for 8.7 keV Beam

The initial radial distribution for the 38 keV beam is shown on the bottom graph of Figure 6. Initial distribution 3 is the distribution for the case neglecting wave-particle effects. Initial distribution 4 is the distribution for the case including the effects of wave-particle interactions. Other parameters pertinent to the 38 keV MCBE calculations are summarized in Table 4 below. Since the 38 keV beam is assumed to be warm by us, Equation (16) rather than WPDIF was used to generate the distribution which has been placed in histogram form for input to MCBE.

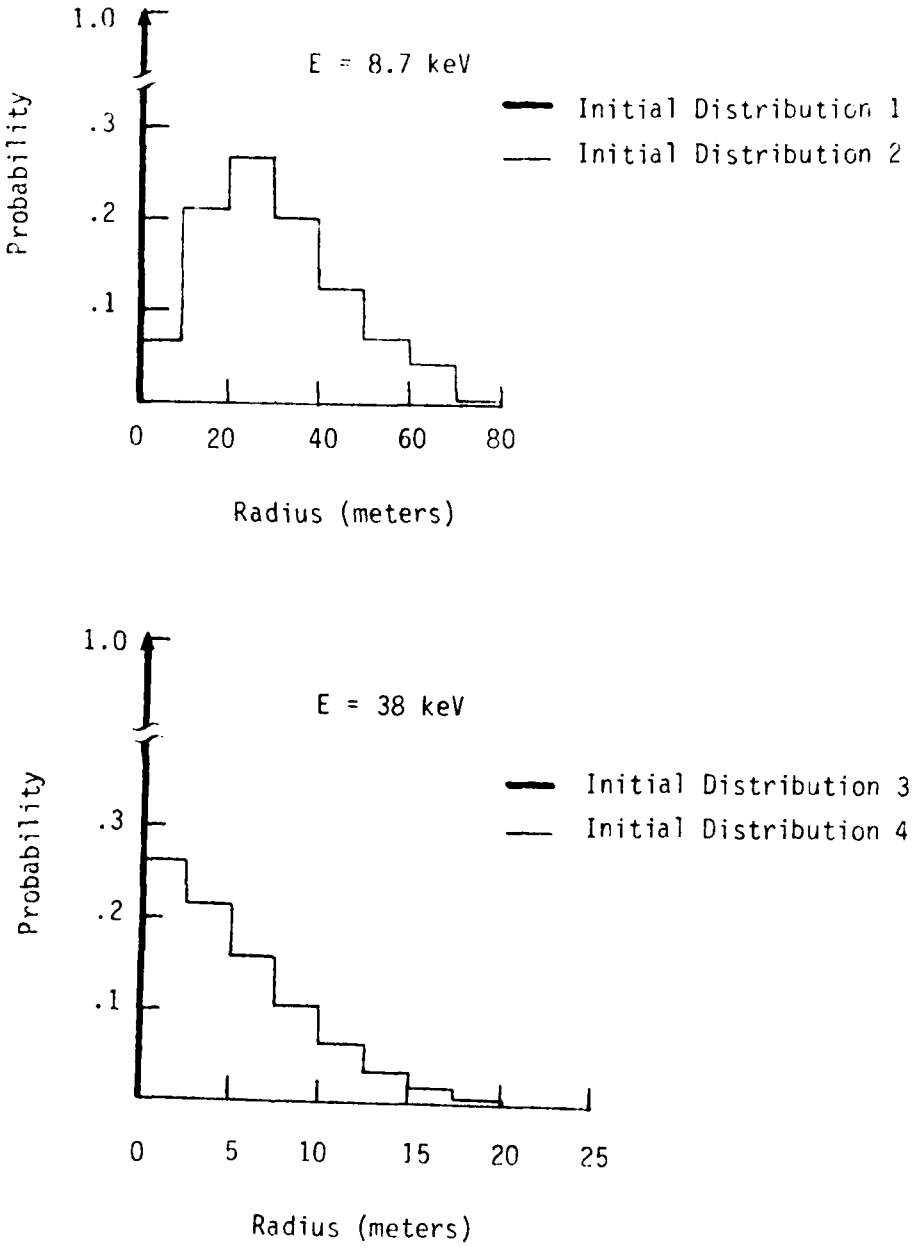

Figure 6. Initial Distribution of Radial Positions Used for the Calculations.

	Neglecting Wave-Particle Effects	Including Wave-Particle Effects
Distribution	3	4
Initial Altitude	212 km	165 km
Initial Angle	70° wrt $\vec{B}_{earth}$	70° wrt $\vec{B}_{earth}$
$\|B_{earth}\|$	.5 gauss	.5 gauss

Table 4. Summary of the Input Parameters for the 38 keV Beam

4.2 MCBE Results.

In this section we present selected results from the MCBE calculations. For the 38 keV beam, the assumption that wave-particle effects and particle-particle effects dominate in different regimes should be valid. The region in which wave-particle effects are predicted to dominate is above 160 km and the energy deposition due to particle-particle effects is negligible at that altitude.

The contour plot of the energy deposition $\dot{D}(z,r)[eV/cm^3\text{-}e]$ for the 38 keV beam is shown in Figure 7. For the case which includes wave-particle interactions, the contour line for a given level extends slightly further out in radius and the peak occurs (within the statistical uncertainty of the results) at the same altitude. Shown in Figure 8 is a plot of the mean radius of energy deposition as a function of altitude. The calculation which includes wave-particle effects shows an overall larger mean radius with a maximum difference of less than 20. at approximately 89 kilometers. Figures 9 and 10 show the column energy deposition versus tangent point distance at 91.5 and 115 km for the 38 keV beam. The Column deposition $D_c(z,r_\perp)$ $[eV/cm^2 - e]$ is obtained by an integration through and perpendicular to the beam. We may thus

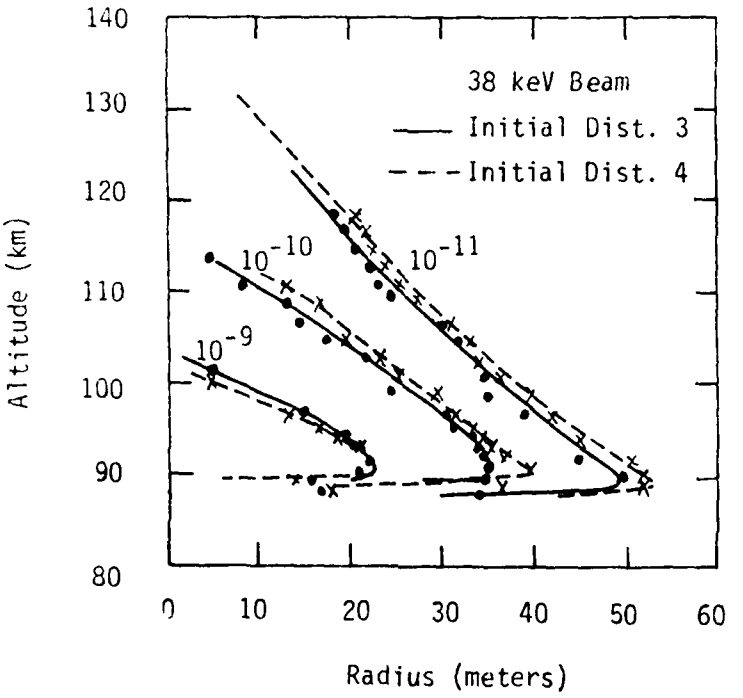

Figure 7. Contour Plots of Energy Deposition for a 38 keV Beam (units eV/cm^3 - e).

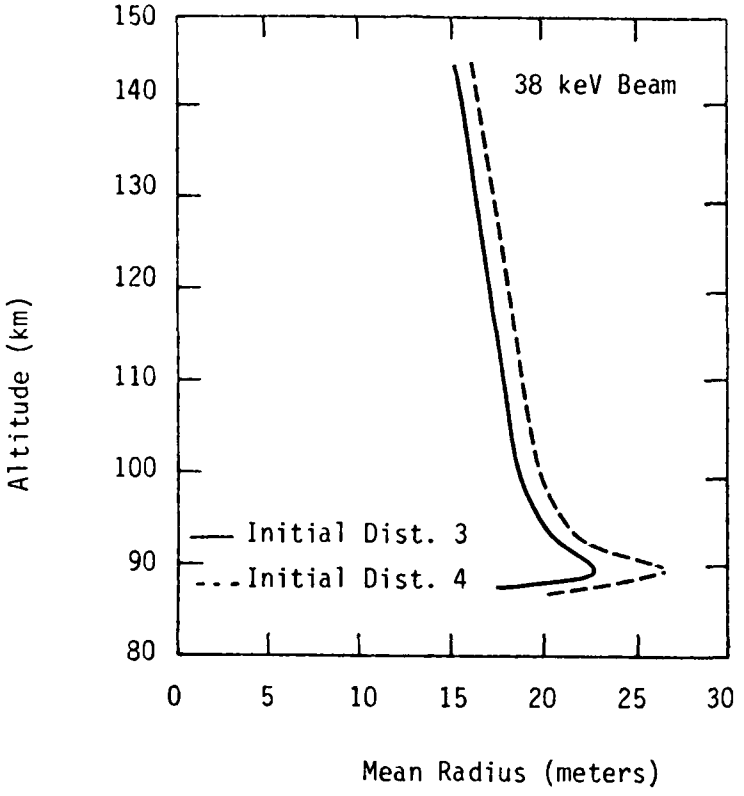

Figure 8. Mean Radius of Energy Deposition Versus Altitude for a 38 keV Beam.

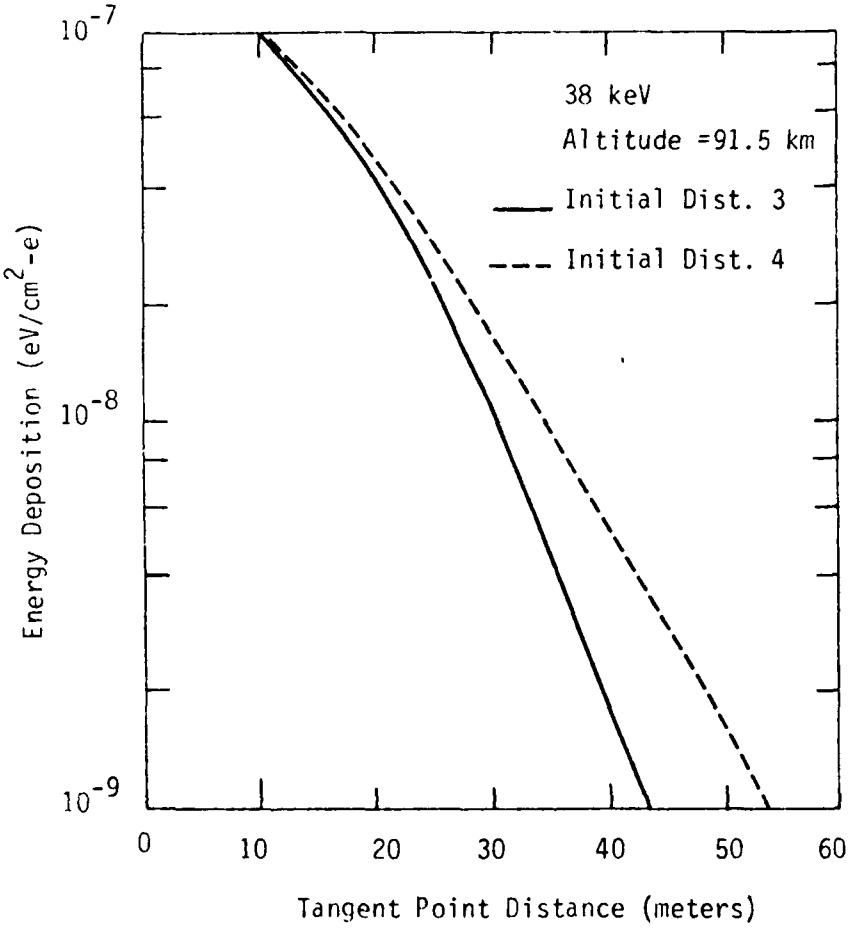

Figure 9. Column Energy Deposition Versus Tangent Point Distance at an Altitude of 91.5 km for a 38 keV Beam.

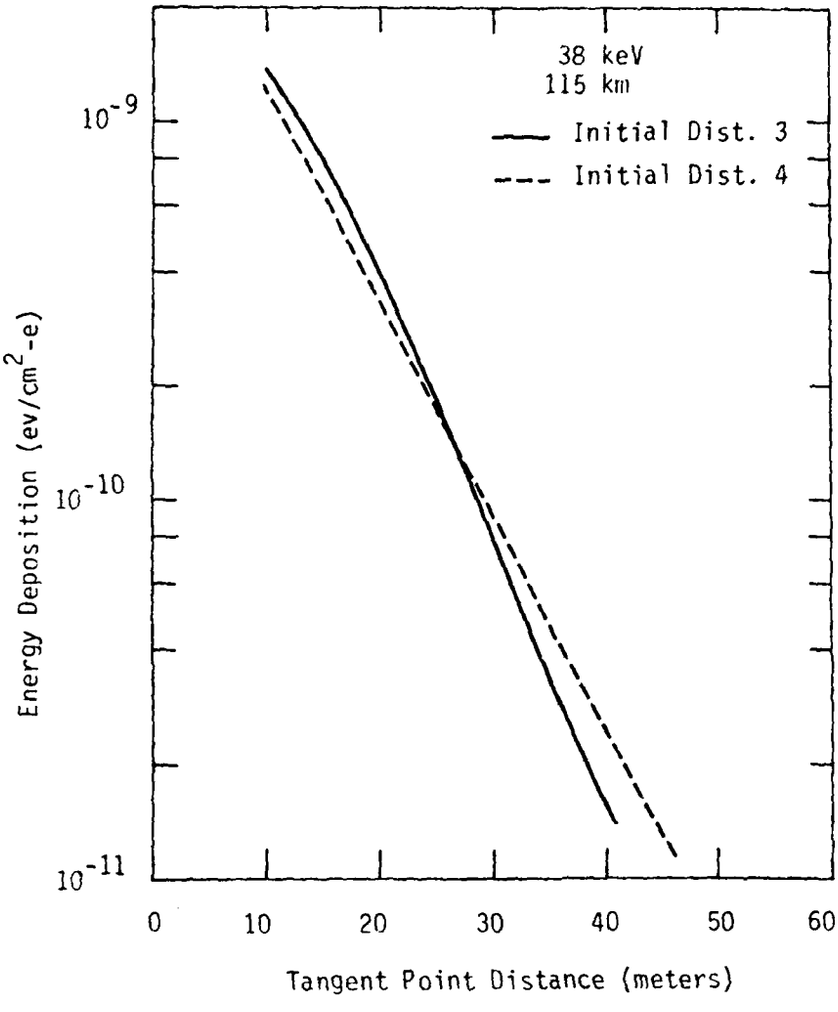

Figure 10. Column Energy Deposition Versus Tangent Point Distance at a Altitude of 115 km for a 38 keV Beam.

view this quantity as being projected onto a plane parallel to the beam axis. In the next subsection, we will discuss how the column deposition may be related to various optical emission features. Upon transforming deposition to emission, results like those in Figures 9 and 10 give brightness of a beam streak in two dimensions.

For the case of the 8.7 keV beam, there is an overlap between the altitude regimes in which the wave-particle and the particle-particle effects are important. The WPDIF calculation for this case indicates that the altitude region for which wave-particle effects are important extends below 110 km. There is substantial energy deposition for particle-particle effects above 110 km, however, and it was necessary to seek a compromise in order to apply the techniques to this case. An altitude of 120 km was chosen as the altitude at which to terminate the WPDIF calculation and begin the MCBE calculation.

Shown in Figure 11 is a contour plot of energy deposition for the 8.7 keV beam. From this plot, one can see that the energy is deposited over a much larger volume for the case in which wave-particle interactions are included. Note the absence of the 10^{-9} contour level for this case.

Figure 12 shows that the mean radius of energy deposition is about a factor of four greater for the case in which wave-particle interactions are included. Figures 13 and 14 show the column energy deposition versus tangent point distance at 105 and 115 km for the 8.7 keV beam.

4.3 Optical Properties.

In this sub-section, we relate the column energy deposition rate such as shown in Figures 9, 10, 13, and 14 to optical emission properties. This will enable us to estimate the brightness of e-beam produced optical streaks as might be seen by a distant optical imaging system. The reference

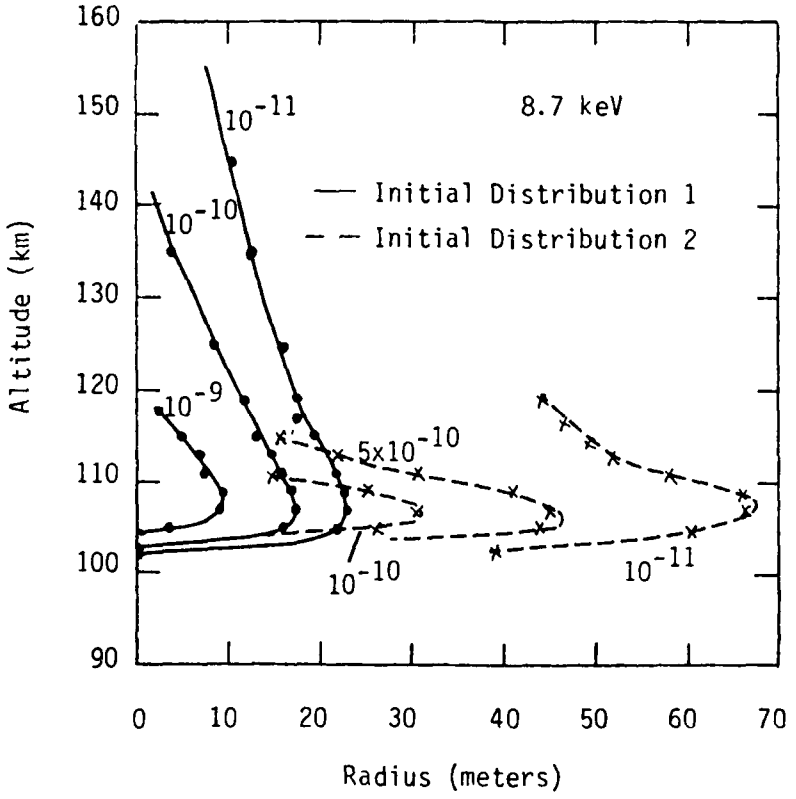

Figure 11. Contour Plots of Energy Deposition for a 8.7 keV Beam (units are eV/cm^3-e)

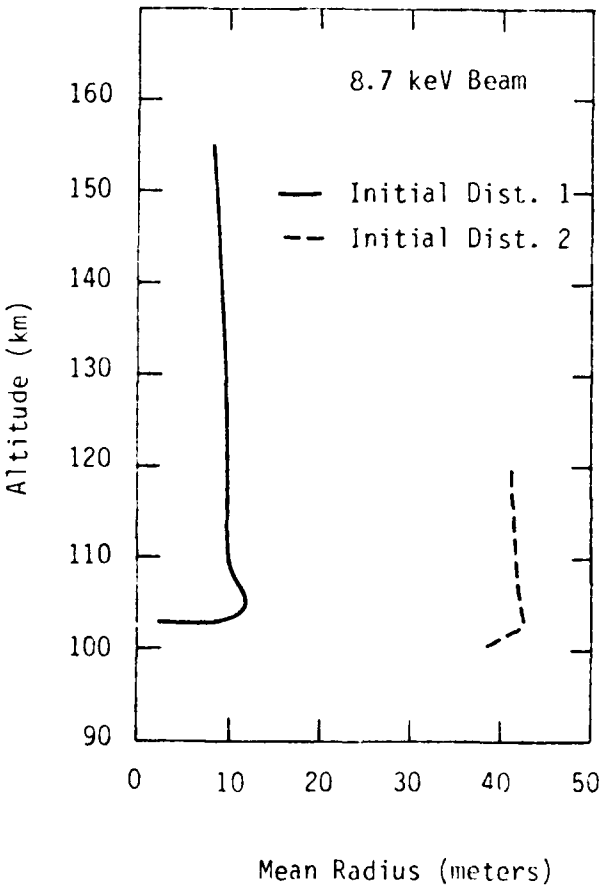

Figure 12. Mean Radius of Energy Deposition Versus Altitude for a 8.7 keV Beam.

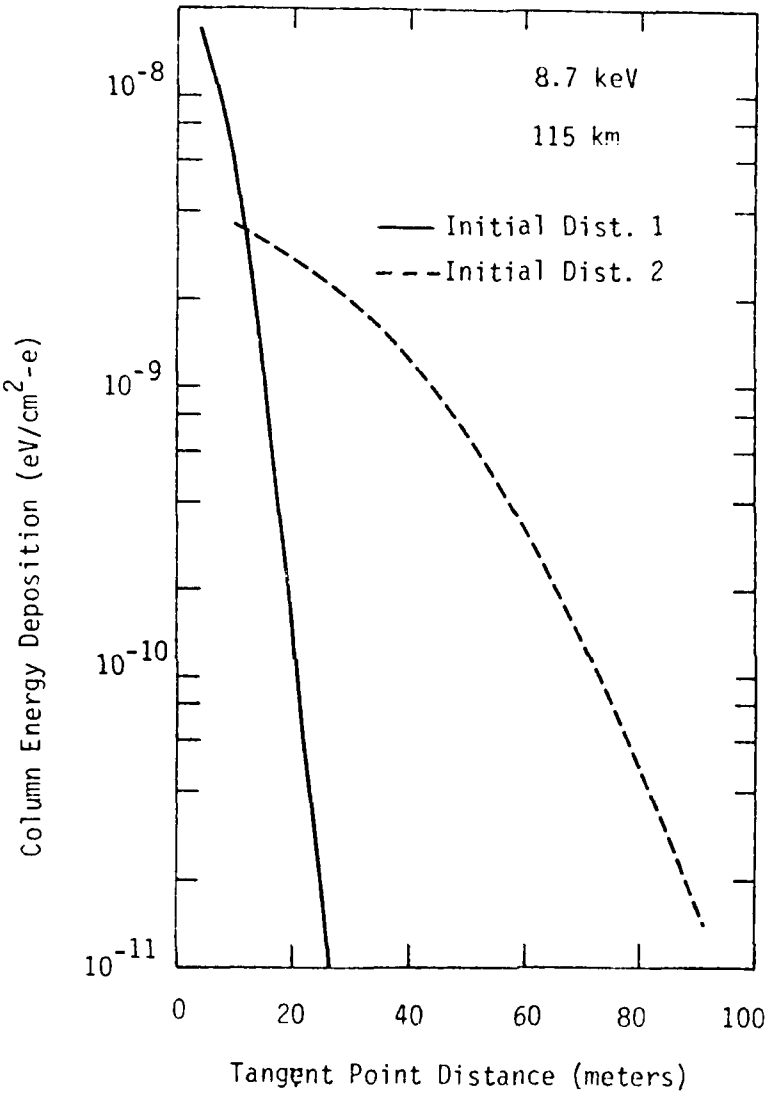

Figure 13. Column Energy Deposition Versus Tangent Point Distance at an Altitude of 115 km for an 8.7 keV Beam.

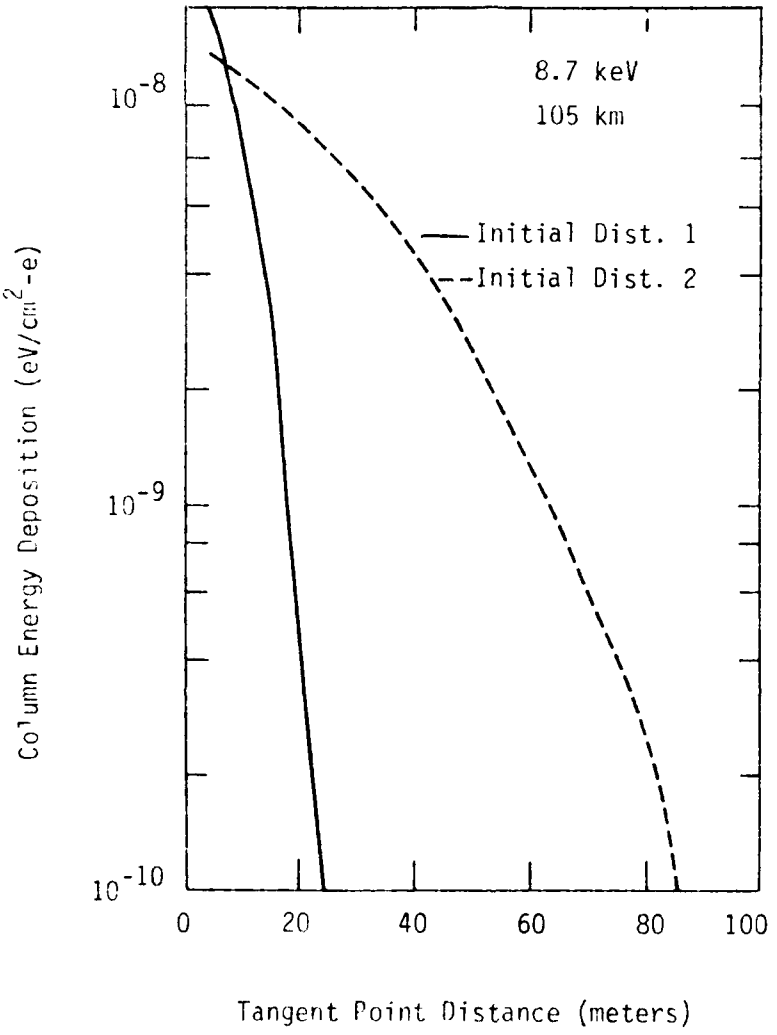

Figure 14. Column Energy Deposition Versus Tangent Point Distance at an Altitude of 105 km for an 8.7 keV Beam.

material for the optical aspects of the discussion to follow come from Vallance Jones (1974) and O'Neil et al. (1978).

EMISSION FEATURES

We have chosen to examine the spectral region between ~ 3200 A and 8500 A. Table 5 provides a list of some of the more prominent features in this range with estimates of their strengths relative to that of N_2^+ 1N 3914 A (Vallance Jones (1974)). The spectrum becomes more complicated at the longer wavelengths which is the reason we have not included features in the table for such wavelengths.

EMISSION FACTORS

We designate the emission factor f through the following relationship:

$$4\pi I(z,r_\perp) = 6.25 \times 10^{12}\ f J D_c(z,r_\perp) \quad \text{Rayleighs } (10^6 \text{ ph/cm}^2 - \text{s} - 4\pi \text{ sr}) \qquad (36)$$

where $4\pi I$ is the column emission rate, J is the starting beam current in amps, and the constant provides the proper scaling to give Rayleighs.

Examples of f-values are given in Table 6. Values are shown for individual prominent features, partial and entire band systems, and the total of the systems considered for wavelengths less than 8500 A. The given value for 3914 A provides an efficiency of 5.4×10^{-3} (energy emitted/energy deposited). Assuming 10% of the incident beam energy is backscattered, this number gives an efficiency relative to the incident beam energy of 4.9×10^{-4} which is close to the value obtained by O'Neil, et al. (1978).

(A)	FEATURE	EMISSION STRENGTH
3370	N_2 2P (0,0)	30
3536	(1,2)	7
3576	(0,1)	20
3582	N_2^+ 1N (1,0)	7
3709	N_2 2P (2,4)	2
3754	N_2^+ 1N (1,3)	6
3804	(0,2)	8
3884	(1,1)	4
3914	(0,0)	100
3997	N_2 2P (1,4)	4
4058	(0,3)	3
4236	N_2^+ 1N (1,2)	4
4278	(0,1)	30
4709	(0,2)	6
5577	OI (^1S - ^1D)	100
6300	OI (^1D - ^3P)	VARIABLE

Table 5. Prominent UV to Middle UV Features
And Their Emission Strengths Relative To
100 Units Of N_2^+ 1N 3914 A

FEATURE	EMISSION FACTOR
3914 A	1.7 (- 3)
N_2^+ 1N SYSTEM	2.6 (- 3)
OI 5577 A	1.7 (- 3)
2P 3370 A	5.6 (- 4)
2P 3576 A	3.3 (- 4)
N_2 2P SYSTEM	1.9 (- 3)
N_2 1P SYSTEM (<8500 A)	5.0 (- 3)
N_2 VK SYSTEM	8.3 (- 4)
N_2^+ M (<8500 A)	2.8 (- 3)
TOTAL (SYSTEMS PLUS OI 5577 A)	1.4 (- 2)

Table 6. Approximate Emission Factors For Prominent Lines, Bands, And Band Systems Within The Interval From ~3200 A To 8500 A

The 3914 A f-value just discussed was obtained from:

$$f_{3914} = \frac{1}{34} \frac{0.8[N_2]}{0.8[N_2] + [O_2] + 0.5[O]} \frac{1}{14} \tag{37}$$

where 34 is the applied eV/ion pair value, the weighted density ratio gives the relative N_2^+ ionization, and 14 is the applied ratio of N_2^+ ions to 3914 A photons. The formula has been applied to the 100 km region where [O] is unimportant.

The emission factors other than for 3914 A in Table 6 were obtained using Tables 4.5 and 4.9 - 4.13 from Vallance Jones (1974). All such values are relative to f_{3914}.

It is worthwhile estimating the efficiency of all features considered in Table 6. To do so, let us assume an average wavelength of 5000 A which corresponds to an energy of 2.5 eV. This yields an efficiency of 3.8% (energy/incident beam energy) allowing from 10% energy backscatter. This can be compared with experiment using the data of O'Neil, et al. (1978). Given that the beam power was 2 kW we estimate an efficiency of $\sim$ 6% from their Figure 9. Considering all uncertainties and the fact that the calculated efficiency was determined for fewer features than present in the measurement, the agreement in efficiencies is satisfactory.

ENERGY DEPOSITION PROPERTIES

To utilize the emission factors in Table 6, we need values of the volume energy deposition $\dot{Q}_c(z,r_\perp)$ as introduced in the previous sub-section. Figure 15 shows the geometry which applies to the determination of this quantity. The needed integration through the deposition region is

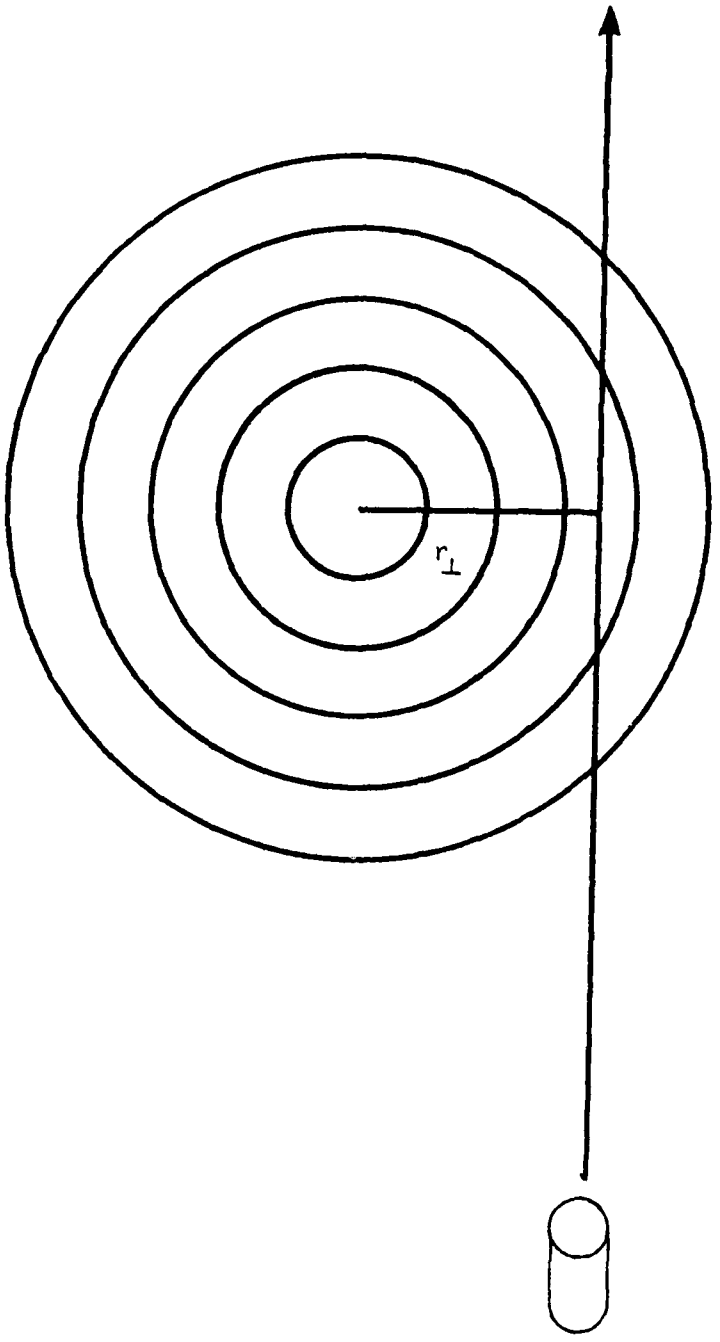

Figure 15. Viewing Geometry

$$D_c(z,r_\perp) = \int \dot{D}(z,r(s))\, ds \quad eV/cm^2\text{-}e \tag{38}$$

where ds is an element of path length along the line-of-sight.

EMISSION RATES

We now apply the information in Table 6 to some of our previous results for an estimation of brightness of an optical streak produced by an e-beam. We choose to consider the 38 keV beam and thus address ourselves to Figures 9 and 10. Attention will be given to the results for wave-particle and particle-particle effects in terms of the sum of features listed in Table 6. The beam current J in Equation (36) is taken to be 50 mA since this is close to the ECHO IV current for the 38 keV shot.

From Equation (36), we then have

$$4\pi I(z,r_\perp) = 4.4 \times 10^9\, D_c(z,r_\perp) \tag{39}$$

Figure 16 shows $4\pi I$ as a function of $r_\perp$ at several altitudes. Emission rates such as these can be used directly to determine the requirements of optical imaging systems being used to determine streak widths. The collection rate of photons by the system is given by:

$$F = \frac{10^6}{4} \frac{A_c}{R^2} \int_z \int_{r_\perp} 4\pi I(z,r_\perp)\, dz\, dr_\perp \quad \text{photons/s} \tag{40}$$

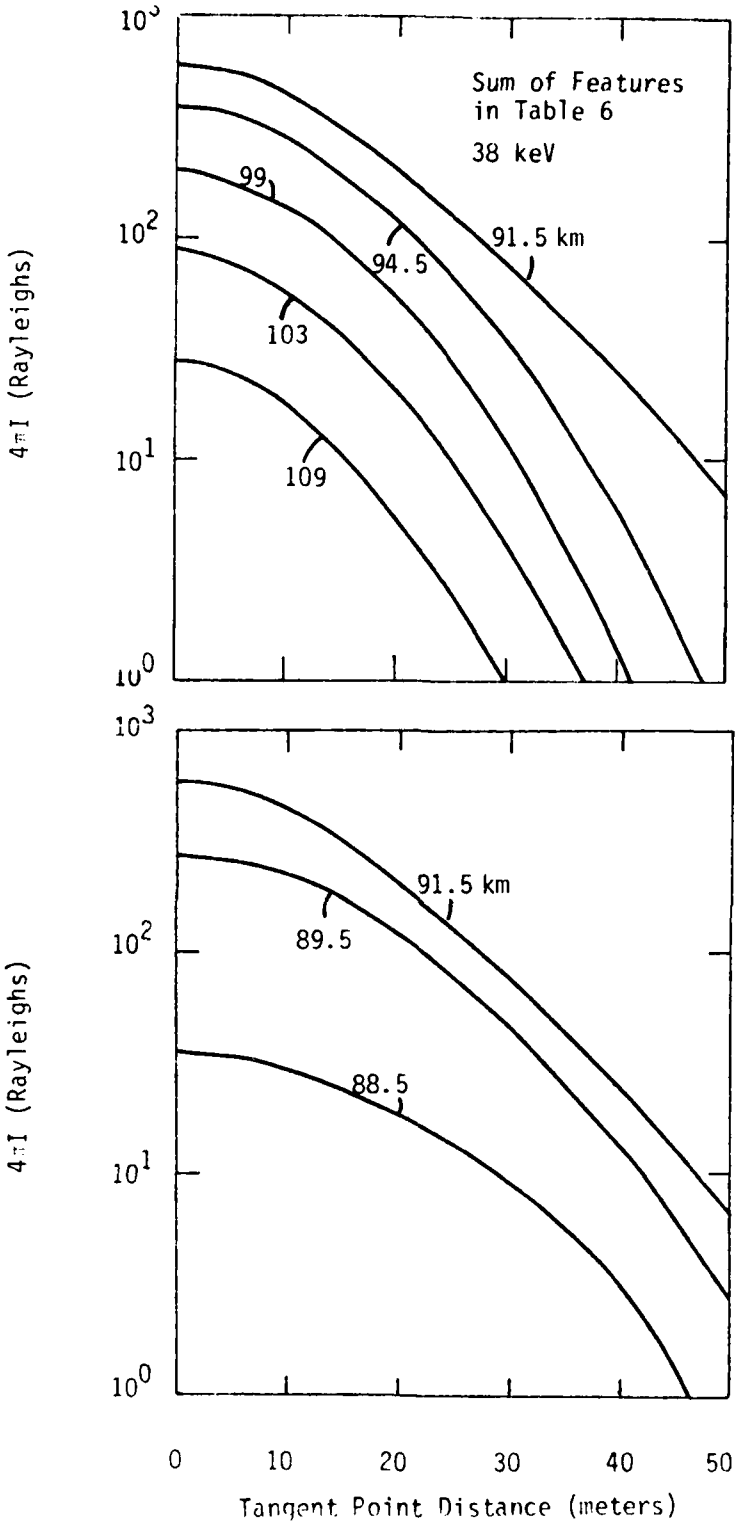

Figure 16. Brightness of Sum of Optical Features in Table 6 Versus Tangent Point Distance. The Upper and Lower Panels Apply Respectively to Altitudes Above and Below 91.5 km for the ECHO IV 38 keV Beam.

where A_C is the collector area, R is the detector-to-streak distance, and Δz and $\Delta r_\perp$ give the surface area of the streak viewed by the detector. As an example, consider the following parameter values:

- R = 120 km
- $\Delta z = \Delta r = 10m$
- $A_C = 100\ cm^2$.

For the brightnesses given in Figure 9, this gives for F, the rather weak value of 31 photon/s from the brightest part of the streak. For the Davis observation, this value should increase almost an order of magnitude since the beam current in that experiment was larger by a corresponding amount compared to that of the ECHO IV 38 keV shot.

Section 5

ACKNOWLEDGEMENTS

We would like to thank Dr. Howard Bloomberg for several useful discussions during the preparation of this manuscript.

REFERENCES

Berger, M.J., "Methods in Computational Physics", 1, 135, Academic Press, New York, 1963.

Berger, M.J., S.M. Seltzer, and K. Maeda, "Energy Deposition by Auroral Electrons in the Atmosphere", J. Atm. and Terr. Phys. 32, 1051, 1970.

Clemmow, P.C., and J.P. Dougherty, "Electrodynamics of Particles and Plasmas", Chapter 9, Addison-Wesley, Reading, Mass., 1969.

Davidson, R.C., "Methods in Nonlinear Plasmas", Chapters 4, 8, and 9, Academic Press, New York, 1972.

Davis, T.N., T.J. Hallinan, C.D. Mead, J.M. Mead, M.C. Trichel, and W.N. Hess, "Artificial Aurora Experiment: Ground-Based Optical Observations", J. Geophys. Res., 76, 6082, 1971.

Drummond, W.E., J.J.H. Malmberg, T.M. O'Neil, and J.R. Thompson, "Nonlinear Development of the Beam-Plasma Instability" Phys. Fluids, 13, 2422, 1970.

Farley, D.T., "A Plasma Instability Resulting in Field Aligned Irregularties in the Ionosphere", J. Geophys. Res., 68, 6083, 1963.

Hallinan, T.J., H.C. Stenback-Nielsen, and J.R. Winckler, "The ECHO IV Electron Beam Experiment: Television Observation of Artificial Auroral Streaks Indicating Strong Beam Interactions in the High-Latitude Magnetosphere", J. Geophys. Res., 83, 3263, 1978.

Lin, D.L., and D.J. Strickland, "Determination of Artificial Auroral Streak Widths", J. Geophys. Res., 86, 4763, 1981.

O'Neil., T.M, and J.H. Malmberg, "Transition of the Dispersion Roots From Beam-Type to Landau-Type Solutions:, Phys. Fluids, 11, 1754, 1968.

O'Neil, T.M., J.H. Winfrey, and J.H. Malmberg, "Nonlinear Interaction of a Small Cold Beam and a Plasma", Phys. Fluids, 14, 1204, 1971.

O'Niel, R.R., F. Bien, D. Burt, J.A. Sandock, and A.T. Stair, Jr., "Summarized Results of the Artificial Auroral Experiment, Precede", J. Geophys. Res., 83, 3273, 1978.

Stix, T.H., "Energetic Electrons From a Beam-Plasma Overstability", Phys. Fluids, 7, 1960, 1964.

Stix, T.H., "The Theory of Plasma Waves", Chap. 8, Mc-Graw-Hill, N.Y., 1962.

Tsytovich, V.N., "Theory of Turbulent Plasma", Consultants Bureau, N.Y., p. 154, 1977.

Appendix A

DERIVATION OF LINEAR GROWTH RATE

The best developed branch of plasma physics is linear instability theory because of its mathematical tractability. Linear instability theory can identify those modes in a plasma that will go unstable and gives the frequency and vector wave number of the mode. The theory of plasma turbulence is the attempt to understand how these linearly unstable modes saturate. In this section, we develop the appropriate linear dispersion relation for this problem and quote some of the pertinent results.

The pertinent plasma linear instability theory for this report starts with the Valsov equation and linearizes about a perturbed electric field. The relevant equations for this problem are:

$$\frac{\partial f_j}{\partial t} + \underline{v} \cdot \frac{\partial f_j}{\partial \underline{x}} + \frac{e_j}{M_j}\left[\underline{E} + (\underline{v} \times \underline{B})\right] \cdot \frac{\partial f_j}{\partial \underline{v}}$$

$$= -\nu_j \; f_j - \frac{N_j}{N_{0j}} f_0^j \quad , \qquad (A.1)$$

$$\frac{\partial \underline{E}}{\partial \underline{x}} = \sum_j e_j \int_{-\infty}^{\infty} f_j \, d^3 v \quad . \qquad (A.2)$$

where:

$f_j(\underline{x}, \underline{v}, t)$ = probability distribution function for j^{th} species as a function of position, velocity, and time;

$\underline{E}$ = electric field;

$\underline{B}$ = magnetic field;

e_j = charge of the j^{th} species;

M_j = mass of the j^{th} species;

N_j = j^{th} species particle density = $\int d\underline{v} f_j$;

N_{0j} = unperturbed j^{th} species particle density; and

ν_j = j^{th} species - neutral collision frequency.

The righthand side of Equation (A.1) is the so-called BGK collision term (Farley (1963)) and has been demonstrated to adequately represent the effect of charge particle-neutral collisions on linear growth rates. Of course, Equation (A.2) is just Poisson's equation.

Equations (A.1) and (A.2) are linearized by assuming:

$$\underline{B}(\underline{x},t) = B_0(\underline{x},t)\hat{z};$$

$$E(\underline{x},t) = \hat{k}E(\underline{k},\omega)e^{iA} \text{ (electrostatic approximation)};$$

$$f_j(\underline{x},\underline{v},t) = f_{j0}(\underline{v}) + \tilde{f}_1(\underline{k},\underline{v},\omega)e^{iA};$$

$$f_{0j}(\underline{v}) = N_{j0}(\eta_j/\pi)^{3/2} e^{\eta_j|\underline{v} - \underline{v}_{0j}|^2};$$

where:

$$\frac{1}{\eta_j} = \frac{2k_B T_j}{M_j} = 2v_{thj}^2 = \text{thermal velocity squared;}$$

$$A = (\omega - \underline{k} \cdot \underline{x});$$

ω = radial wave frequency;

$\underline{k}$ = wave number;

v_{0j} = drift velocity of j^{th} species.

To make this standard electrostatic perturbation fit the problem at hand, we also assume we have three species:

(1) plasma ions (i),

(2) plasma electrons (e), and

(3) beam electrons (B).

The beam electrons have a net motion in the $\hat{Z}$ direction:

$$\underline{v}_{0i} = 0;$$

$$\underline{v}_{0e} = 0; \text{ and}$$

$$\underline{v}_{0B} = v_Z \hat{Z}$$

Under these assumptions, the first order equation from Equation (A.1) can be written:

$$\frac{D}{Dt}\left[f_j(\underline{k},\underline{v},\omega)e^{iA} \right] = \left[\frac{e_j}{M_j} E(\underline{k},\omega) f_{0j}(\underline{v}) - \nu_j \frac{N_j}{N_{0j}} f_{0j}(\underline{v}) \right] e^{iA} \quad (A.3)$$

where:

$$\frac{D}{Dt} \equiv \left[\frac{\partial}{\partial t} + \underline{v} \cdot \frac{\partial}{\partial \mathbf{x}} + \frac{e_j}{M_j} (\underline{v} \times \underline{B}) \frac{\partial}{\partial v} + \nu_j \right] . \quad (A.4)$$

Equation (A.3) can be solved for $f_i(\underline{k},\underline{v},\omega)$ by integrating over the unperturbed orbit defined by the operator, Equation (A.1). $f_j(\underline{k},\underline{v},\omega)$ can then be integrated over velocity as prescribed by Equation (A.2) to obtain a linear dispersion relation. This procedure is well documented in several sources, for example, Clemmow and Dougherty (1969) and Stix (1962). The final result of this procedure is:

$$1 + \sum_j H_j(\omega,\underline{k}) = 0 \quad , \quad (A.5)$$

$$H_j(\omega,\underline{k}) = - \frac{\omega_{pj}^2}{k^2 v_{thj}^2} \frac{1 + i\omega_j^* G_j(\omega,\underline{k})}{1 - \nu_j G_j(\omega,\underline{k})} \quad , \quad (A.6)$$

$$G_j(\omega,\underline{k}) = \frac{-i}{\sqrt{2} v_{thj} k_Z} e^{-\lambda_j} \sum_{n=-\infty}^{\infty} I_n(\lambda_j) Z(\zeta_{jn}) \quad ; \quad (A.7)$$

where:

$\omega_{pj}^2 = 4\pi n_j e_j^2/M_j$ = plasma frequency;

$\omega_j^* = \omega + i\nu_j - k_Z v_Z$;

$\zeta_{nj} = 1/\sqrt{2\, k_Z\, v_{thj}}\,(\omega_j^* - n\Omega_j)$ thermal velocity;

$\lambda_j = (v_{thj}/\Omega_j\, k_\perp)^2$;

$k_\perp$ = k vector perpendicular to B-field;

k_Z = k vector parallel to B-field;

I_n = n^{th} modified Bessel function; and

Z = plasma dispersion function
Fried and Conte (1969).

G_j [Equation (A.7)] is known as the Gordeyev integral, Clemmow and Dougherty (1969). To extract a meaningful amount of information from Equation (A.5), the usual "cold" plasma limit is taken. This limit is:

$$\left.\begin{array}{ll} \lambda_j << 1 & , \\ |\zeta_{jn}| >> 1 & , \\ \omega_{pj} >> \nu_j & , \end{array}\right\} \quad (A.8)$$

which is equivalent to saying $kv_{thj} << \omega_j, \Omega_j$, and collisions are negligible. In this limit, only the $n = -1, 0, +1$ terms in Equation (A.6) are retained and the Bessel function and plasma dispersion function are expanded by the following prescription (Abramowitz and Stegun (1964)):

$$I_n(\lambda) \cong \frac{1}{(2\lambda)^n} \quad ,$$

$$Z(\zeta) \cong -\frac{1}{\zeta}\left(1 + \frac{1}{2\zeta^2}\right) \quad .$$

These expansions led to the following result for H_j when $j = i, e$:

$$H_j(\omega,k) = -\frac{k^2}{k^2}\left(\frac{\omega_{pj}^2}{\omega^{*2} - \Omega_j^2}\right) - \frac{k_Z^2}{k^2}\left(\frac{\omega_{pj}^2}{\omega^{*2}}\right) \quad . \qquad (A.9)$$

The limit [Equation (A.8)] is, however, not valid for the beam electrons. In this case, it will turn out, the electrostatic perturbations of interest will process the following property:

$$\zeta_{Bo} = \left|\frac{\omega - i\nu_B - k_Z v_Z}{k_Z v_j}\right| << 1 \quad . \qquad (A.10)$$

For this scaling, the Landau prescription for expanding the plasma dispersion function is operative (Stix (1964)), and leads to the result:

$$H_B(\omega,\underline{k}) = i\varepsilon_B = -i\,\frac{k_Z}{k^3}\,\omega_{pB}^2\,\frac{f'_{0B}(\omega/k_Z)}{n_B} \quad . \qquad (A.11)$$

Combining the approximations of Equations (A.9) and (A.11) into the plasma dispersion relation, Equation (A.5), and neglecting the ion contribution ($\omega_{pe}^2 >> \omega_{pi}^2$), we obtain:

$$1 + \frac{k^2}{k^2}\left(\frac{\omega_{pe}^2}{\omega^2-\Omega_e^2}\right) + \frac{k_Z^2}{k^2}\left(\frac{\omega_{pe}^2}{\omega^2}\right) = i\varepsilon_B \quad . \qquad (A.12)$$

Equation (A.12) is the standard approximate dispersion relation for this two stream or bump on tail instability. When this approximation is legitimate and the growth rate is much less than the real part of the frequency:

$$\omega = \omega_R + i\gamma, \quad \omega_R >> \gamma \quad ,$$

where γ = growth rate, Equation (A.12) can readily be solved by first setting γ, ε_B to zero and solving for ω_R; then expanding the right-hand side in terms of γ and equating it to ε_B.

The result of these manipulations are:

$$\gamma = \frac{\Omega}{2}\left[\frac{\omega^2\varepsilon_B}{k_Z^2\omega_{pe}^2}\right]Q(\omega) \quad , \qquad (A.13)$$

$$Q(\omega) = \frac{\omega(\omega^2-\Omega^2)(\omega^2-\Omega^2-\omega_p^2)}{\Omega_e^3(2\omega^2-\Omega^2-\omega_p^2)} \quad , \qquad (A.14)$$

$$\frac{k_\perp^2}{k_Z^2} = -\frac{(\omega^2-\Omega^2)(\omega^2-\omega_p^2)}{\omega^2(\omega^2-\Omega^2-\omega_p^2)} \quad , \qquad (A.15)$$

where we have to drop the "e" subscript and redefine $\omega_R \equiv \omega$. As always, it is argued that the dominance to oscillation will be the one with the largest growth rate. The procedure is to maximize $Q(\omega)$ given an Ω and ω_p. This is graphically worked out in Figure 17. Assuming $n_e = 10^5$ cm^{-3} and $B_0 = 0.58$ gauss, we have:

$$\Omega = \frac{eB}{M_e c} = 10^7 \text{ sec}^{-1};$$

$$\omega_p = \frac{4\pi n_e e^2}{M_e} = 1.66 \times 10^7 \text{ sec}^{-1};$$

$$\left(\frac{\omega_p}{\Omega}\right)^2 = 2.75;$$

$$\frac{\omega}{\Omega} = 0.6 \quad \text{(see Figure 17)}$$

$$\omega = 6.0 \times 10^6 \text{ sec}^{-1}.$$

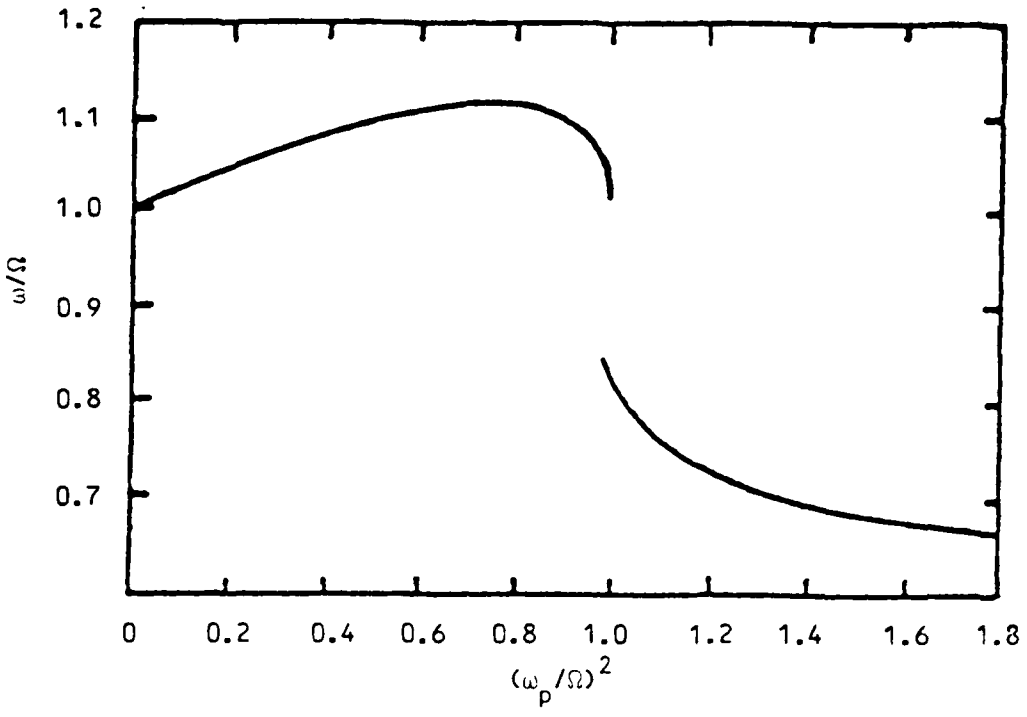

FIGURE 17 ω as a Function of ω_p/Ω to Maximize $Q(\omega)$ in Equation A.13

(Stix (1964))

Using this value of ω in Equation (A.13) gives:

$$Q_{max}(\omega) = 0.4 \quad .$$

Next, ε_B is maximized by choosing an appropriate k_Z [see Equation (A.13)]. This is approximately accomplished by setting:

$$\frac{\omega}{k_Z} \cong v_Z - v_{thB} \quad . \qquad (A.16)$$

In the limit, $v_{thB} << v_Z$, Equation (A.16) can be used in Equation (A.11) to transform Equation (A.13) into:

$$\gamma = 0.76\ \Omega\ \alpha \left(\frac{v_Z^2}{v_{thB}^2} \right) Q_{max}(\omega) \quad , \qquad (A.17)$$

where $\alpha \equiv n_B/n_e$. Of course, the ratio $k_\perp/k_Z$ is determined by Equation (A.15) once ω is chosen to maximize $Q(\omega)$. This ratio is shown in Figure 18 as a function of (ω_p/Ω). For our analysis:

$$\left(\frac{k_\perp}{k_Z} \right)^2 = 1.0 \quad ,$$

which translates into an angle of $\theta_I = 45^o$, where θ_I is the angle between $\underline{k}$ and $\underline{B}$.

The question this analysis does not answer is the effect of collisions on the instability. Roughly speaking, we can see the effect in the expansion condition Equation (A.10). With negligible collisions, the expansion (A.11) was with respect to:

$$\left| \frac{\omega_R + i\gamma + k_Z v_Z}{k_Z v_{thB}} \right| << 1 \quad .$$

Obviously, if we substituted $i\nu_B = i\gamma$ in the computation for $H_B(\omega,\underline{k})$, we would get the same numerical answer. Thus, a quick and dirty approximation such that collision frequencies cut off this instability would be the condition:

$$\gamma = \nu_B \quad . \qquad (A.18)$$

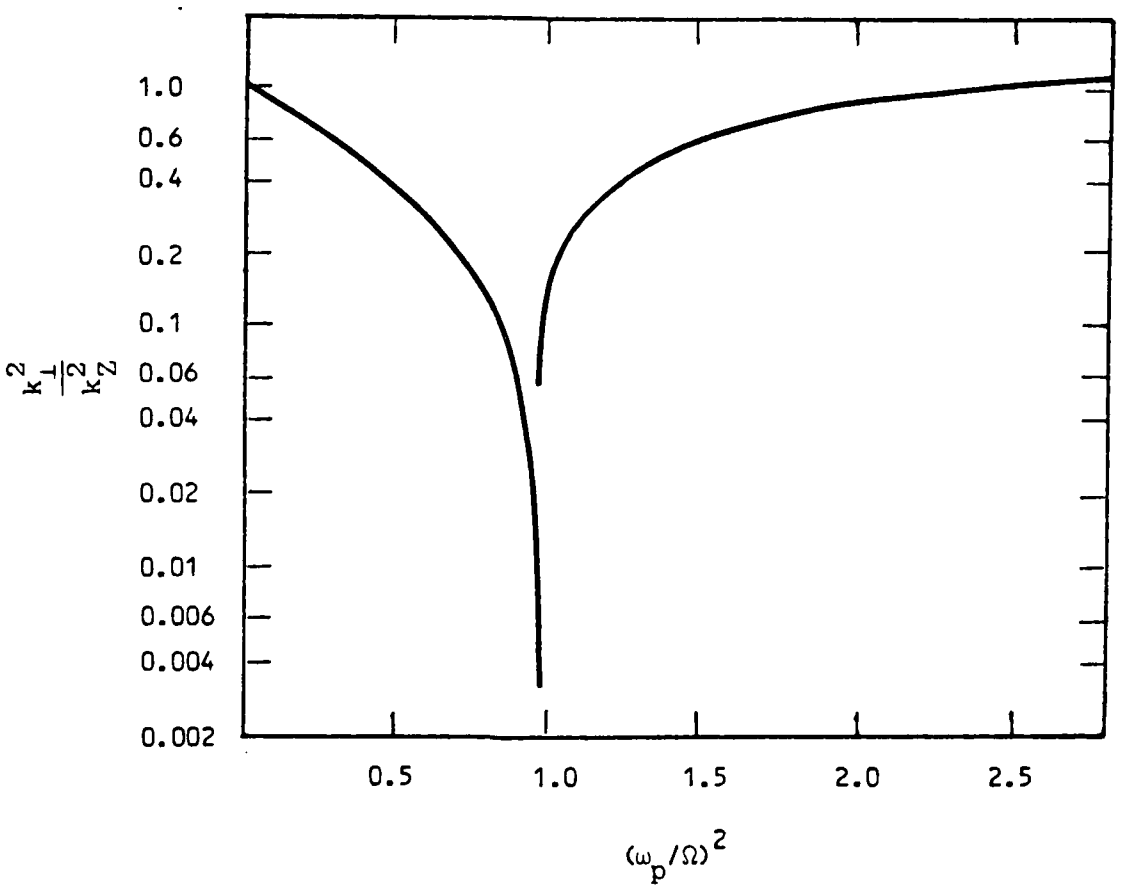

FIGURE 18. Ratio of Perpendicular to Parallel Electric Field that Corresponds to Maximum Q in Equation (A.14)
(Stix (1964))

This is really an argument that the instability will stabilize with the growth rate which is of the same order as the collision frequency. This completely neglects the contribution of the denominators in Equation (A.7). A more precise statement would require the numerical solution of the exact dispersion relation, which is a reasonably tractable computational problem.

Appendix B

DEFINITION OF COHERENCE TIME

To explain the diffusion of auroral streaks, we hypothesize the linear unstable waves introduced in Section 3 grow and saturate to some level of turbulence, producing an E-field that makes the particles $\underline{E} \times \underline{B}$ drift perpendicular to the axis of the beam. The turbulence is pictured as separate regions of coherence, where within each region a definite electrostatic wave eixsts with a particular ω and $\underline{k}$ nominally of the value predicted by the linear theory. If the beam particles traverse these regions experiencing a reasonable constant E-field per region, the guiding center of the particles will be displaced:

$$\Delta x = v_{drift} \quad \tau_{coh} \quad ,$$

where:

$$v_{drift} = \frac{\underline{E} \times \underline{B}}{cB^2} \; ;$$

τ_{coh} = time particle transverses coherence region; and

c = velocity of light.

In terms of gyro-radius, this Δx can be expressed as:

$$\frac{\Delta x}{r_g} = \frac{eE}{M v_B \sin\theta_B} \tau_{coh} \quad . \qquad (B.1)$$

Using this random displacement, the radial diffusion of the electron beam can readily be computed. The objective of turbulence theory is to calculate the coherence time and the magnitude of the E -field.

COHERENCE TIME

To estimate coherence time, we estimate the length of the coherence region. To see how this works, consider Figure 19. Part (a) of Figure 19 is a picture of a spatially uniform wave. From Section 2, we know this wave has wave fronts that move with velocity $(\omega/k) = v_Z$, the phase velocity. Part (b) shows a wave packet containing the wave in Part (a). The wave fronts in the wave packet still travel at the phase velocity, but the wave packet itself will travel of the group velocity. A beam particle transversing the packet at v_Z will be in step with a wave front, and the time within the packet will be:

$$\tau_{coh} = \frac{L}{|v_Z - v_g|} \quad ,$$

L = coherence region length .

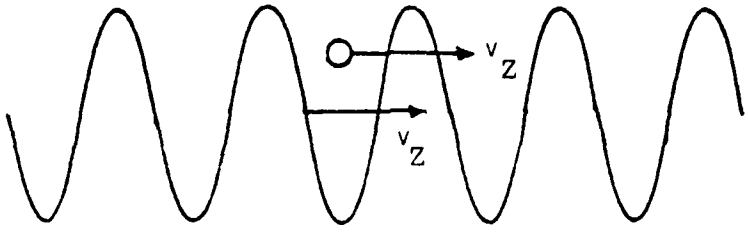

(a)

FIGURE 19(a). Plane Wave with Phase Velocity v_z

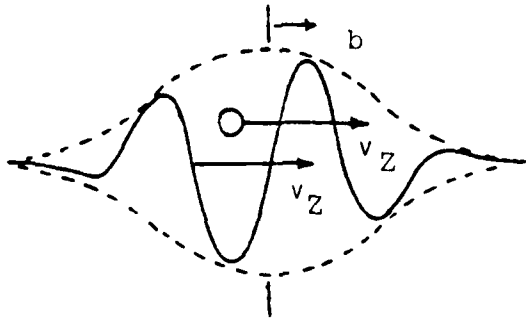

(b)

FIGURE 19(b). Wave Packet with Phase Velocity v_z and Group Velocity v_g

In both pictures, electron velocity is phase velocity; therefore, electrons see constant E-field.

If this picture is valid, the wave packet will have to be at least one wave front wide. Without further justification, we estimate:

$$\tau_{coh} = A_3 \frac{2\pi}{k} \frac{1}{|v_z - v_g|} \; ; \; A_3 \lesssim 1 \qquad (B.2)$$

where A_3 is an arbitrary constant introduced as a measure of the uncertainty in this estimate.

From Equation (3.12), we can show the group velocity along the B-field will be about 0.5 v_z (O'Neil and Malmberg (1968)), so τ_{coh} will be:

$$\tau_{coh} = A_3 \frac{4\pi}{\omega} \quad . \qquad (B.3)$$

Note that this argument justifies the statement that the beam particles will see a constant E-field within a coherence region for any group velocity.

E-FIELD SATURATION

To estimate the E-field saturation, we use two assumptions:

$$\tau_{tr} = A_4 \gamma^{-1} \quad , \qquad A_4 \lesssim 1; \qquad (B.4)$$

$$E^2/8\pi = A_5 n_B k_B T_B \quad , \qquad A_5 \sim 1; \qquad (B.5)$$

where:

$\tau_{tr}^{-2} = k_z e E_z / M$, and

A_4, A_5 = arbitrary constants.

In Equation (B.4), τ_{tr} is referred to as the trapping time. $\tau_{tr}^{-1} = \omega_B$ is the bounce frequency of electrons trapped near the bottom of a spatially oscillating electric field.

A linearly unstable wave grows in a plasma because a reasonable number of beam particles undergo an oscillation in phase with each other. When the trapping time of these particles gets to be of the order of the slowest timescale of the linear instability analysis (the growth rate), the zero order orbits [Equation (B.4)] are modified to the extent the analysis breaks down, hence, Equation (B.1).

Equation (B.5) is a statement that the energy associated with the electric field will scale with the heating of the plasma beam. The more wave fluctuations, the more heating of the plasma beam.

The assumptions, Equations (B.4) and (B.5), are difficult to rigorously justify. They do reproduce the scaling of several 1-D computer simulations and are not contradicted by weak turbulence theory (Davis et al. (1971) and Hallinan et al. (1978)). The advantage of these assumptions is that combined with Equation (A.17), they form a closed set for the calculation of the saturated E-field.

Starting with Equation (B.4), we have:

$$\frac{k_Z^2 e^2 E^2 \cos^2 \theta_I}{M^2} = \left(\frac{\gamma}{A_4}\right)^4 \quad . \qquad (B.6)$$

Letting $k_Z = \omega/v_Z$, we can rewrite Equation (B.6) to read:

$$\frac{E^2}{8\pi} = \frac{\omega^4}{\omega_{pe}^2} \frac{1}{\alpha} \left(\frac{n_B}{2} M v_Z^2\right) \frac{1}{\cos^2 \theta_I} \frac{1}{A_4^4} \quad .$$

Then, using Equation (B.5), we can rewrite the above to read:

$$\left(\frac{\frac{n_B}{2} M v_Z^2}{n_B k_B T} \right) = \frac{\omega^2 \omega_e^2 \alpha}{\gamma^4} \cos^2 \theta_I \, A_4^4 A_5 \quad . \qquad (B.7)$$

Equations (B.4) and (B.7) can now be substituted in Equation (A.17) to obtain:

$$(\gamma / A_4)^2 = \tau_{tr}^{-2} = \left[0.76 \, \Omega Q \, \alpha^2 \omega^2 \omega_e^2 \cos^2 \theta_I \, \frac{A_5}{A_4} \right]^{2/5} \quad . \qquad (B.8)$$

This gives the bounce frequency as a function of parameters derived from linear plasma theory.

BEAM DIFFUSION

Equation (B.8) can now be used to calculate the random step size of the guiding center of beam electrons. From the definition of τ_{tr}, we have

$$\frac{eE_Z}{M v_Z} = \frac{1}{\tau_{tr}^2 \omega} \quad . \qquad (B.9)$$

Substituting the proper angle dependence into Equation (B.9) and using Equations (B.1), (B.3), and (B.8), we can derive:

$$\frac{\Delta x}{r_g} = A_3 \frac{\tan \theta_I}{\tan \theta_B} \frac{4\pi}{\omega^2 \tau_{tr}^2} \quad ,$$

$$\frac{\Delta x}{r_g} = A_3\left(\frac{A_5}{A_4}\right)^{2/5} \frac{4\pi \tan \Theta_I}{\tan \Theta_B} \frac{1}{\omega^2} \left[0.76\, \Omega Q\, \alpha^2 \omega^2 \omega_e^2 \cos^2 \Theta_I\right]^{2/5} . \quad (B.10)$$

Assuming the following parameter values with the Echo IV experiment in mind,

$$\left.\begin{aligned} \Theta_B &= 70^\circ, \\ \Theta_I &= 45^\circ, \\ \omega &= 6.0 \times 10^6 \text{ sec}^{-1}, \\ \Omega &= 1.0 \times 10^7 \text{ sec}^{-1}, \\ \omega_e &= 1.66 \times 10^7 \text{ sec}^{-1}, \\ Q &= 0.4, \end{aligned}\right\} \quad (B.11)$$

we have:

$$\frac{\Delta x}{r_g} = 17.6\, A_3 \left(\frac{A_5}{A_4}\right)^{2/5} \alpha^{4/5} .$$

Then, using Equation (B.1), we can reduce the random step size expression to:

$$\frac{\Delta x}{r_g} = 17.6\, A_3 \left(\frac{A_5}{A_4}\right)^{2/5} \frac{I^{4/5}}{\mathcal{E}_B^{6/5}} \left(\frac{r_B}{r_g}\right)^{8/5} , \quad (B.12)$$

where I is in amps and $\mathcal{E}_B$ is in keV.

COMPARISON WITH EXPERIMENT

Equations (A.17), (B.8), and (B.12) can now be used to compare with the ECHO IV experiment. To make this comparison, we first set our arbitrary constants A_3, A_4, and A_5 equal to unity. These constants indicated the sensitivity of the estimates we made for coherence time, trapping time, and beam thermal spread, respectively.

First, we test the assumption that the instability turns off at 150 km due to electron-neutral collisions. Using Equations (B.8) and (B.11), the growth rate will equal:

$$\gamma = (6.8 \times 10^6)\, \alpha_0^{2/5} \left(\frac{r_g}{r_B}\right)^{4/5} \text{ sec}^{-1} \quad . \quad \text{(B.13)}$$

We now insert into r_B and α_0, their values as estimated for pulse 10 which gave the most diffuse optical streak. These values are taken to be $r_B = 10$ gyro-radii and $\alpha_0 = .00032$ which yield:

$$\gamma = 4.3 \times 10^4 \text{ sec}^{-1} \quad .$$

According to Berger, et al. (1970) this corresponds to a collision frequency at an altitude of 120 km. At 150 km, the collision frequency is 1.2×10^3 sec^{-1}, a factor of 36 lower.

The second assumption we would like to test is the diffusion attributed to the random step size, Equation (B.12). Again, consider pulse 10. For Equation (B.12) with $A_3 = A_4 = A_5 = 1$, we have:

$$\frac{\Delta x}{r_g} = 17.6\ \alpha^{4/5} \quad .$$

Obviously, as the beam descends through the atmosphere, α decreases and this step size will decrease. An overestimate of the beam spreading would be to use a constant step size equal to the initial or maximum step size. In this case, the maximum beam spread will satisfy the inequality:

$$\frac{\Delta r_B}{r_g} < \sqrt{N}\,\frac{\Delta x_{max}}{r_g} = \sqrt{N}\,(17.6\ \alpha_0^{4/5}) \quad , \qquad (B.14)$$

where N is the number of random steps. This can be estimated by:

$$N = \frac{\text{flight time}}{\tau_{coh}} \cong 1.2 \times 10^3 \quad .$$

Thus, an upper bound for streak radius is:

$$\frac{r_B + \Delta r_B}{r_g} < 1.97 \quad ,$$

which is about five times smaller than the observed streak width.


FILMED